MATERIALS AND DEVICES FOR SPINTRONICS APPLICATIONS

by

Nathan Wheeler Gray

A dissertation submitted to the faculty of
The University of Utah
in partial fulfillment of the requirements for the degree of

Doctor of Philosophy

Department of Materials Science and Engineering

University of Utah

December 2011

The University of Utah Graduate School

STATEMENT OF DISSERTATION APPROVAL

The dissertation of **Nathan Wheeler Gray**

has been approved by the following supervisory committee members:

Ashutosh Tiwari	, Chair	**11/22/2011** Date Approved
Feng Liu	, Member	**12/7/2011** Date Approved
Ravi Chandran	, Member	**12/5/2011** Date Approved
Michael Scarpulla	, Member	**11/20/2011** Date Approved
Gerald Stringfellow	, Member	**11/22/2011** Date Approved

and by **Feng Liu** , Chair of

the Department of **Materials Science and Engineering**

and by Charles A. Wight, Dean of The Graduate School.

ABSTRACT

Realization of next generation spintronic devices will require the use of design and engineering of new materials. In order to reach the performance requirements for spintronic transistor devices to become a reality, spin injection must be extremely efficient at room temperature. Understanding new materials and combinations of materials will enable the injection efficiency required for next-generation devices.

Rare earth oxides are explored to determine the feasibility of doping magnetic elements to make new dilute magnetic dielectric materials for spin tunneling injection applications. Samarium Oxide (Sm_2O_3) doped with a small amount of cobalt (Co) is shown to exhibit a magnetic phenomenon which cannot be accounted for by conventional models. Though the observed magnetic properties appear quite similar to those observed in superparamagnetic systems, the origin of these properties is entirely different. A model, based on the widely accepted bound polaron theory for insulating ferromagnets, is proposed to explain the magnetic behavior of Co doped Sm_2O_3 films.

We have also explored the growth and properties of high quality Tb_2O_3 thin films with on a variety of substrates in preparation for magnetic doping. We show enhanced dielectric constant related to improved crystal quality compared with previous reports, which makes this material of interest in high-k applications as well.

Furthermore, we report room-temperature, all-electrical injection and detection of spin-polarized carriers in silicon using NiFe/MgO tunnel-barrier-contacts. From the

magnetic-field dependence of the spin-accumulation voltage, spin-lifetime and diffusion-length of the carriers were determined to be 276 ps and 328 nm, respectively. Attaining spin diffusion lengths of >320 nm in Si channels is a ground breaking step and opens tremendous opportunities for integrating spin functionality into post-Moore-era electronic devices.

We have carried out similar research with ZnO channels. We report all-electrical injection and detection of spin-polarized carriers in ZnO using NiFe/MgO tunnel-barrier-contacts. The three-terminal Hanle effect is used to study spin transport in single crystal thin film ZnO grown on sapphire. The results show that spin injection persists up to and above room temperature, with a measured lifetime τ_s=174 ps at 340K. These results underscore the importance of ZnO as a material for future active spintronics devices.

TABLE OF CONTENTS

LIST OF FIGURES

Figure Page

LIST OF ABBREVIATIONS

2DEG	Two-dimensional electron gas
ALD	Atomic layer deposition
BAP	Bir-Aranov-Pikus spin scattering mechanism
BJT	Bipolar Junction Transistor
CMOS	Complementary metal-oxide semiconductor
DMD	Dilute magnetic dielectric
DMS	Dilute magnetic semiconductor
DP	D'yakonov-Perel spin scattering mechanism
EDS	Energy dispersive x-ray spectroscopy
EY	Elliot-Yafet spin scattering mechanism
FC	Field-cooled
FET	Field effect transistor
GMR	Giant magnetoresistance
HR	High-resolution
IC	Integrated circuit
MRAM	Magnetic random access memory
MIS	metal-insulator-semiconductor
PLD	Pulsed laser deposition
REO	Rare-Earth oxide

SAD	Selected area diffraction
SEM	Scanning electron microscope
SO	Spin-orbit
SQUID	Superconducting quantum interference device
TM	Transition metal
TEM	Transmission electron microscope
TMA	Tri-methyl aluminum
TMR	Tunnel magnetoresistance
UV/Vis	Ultraviolet/Visible
VSM	Vibrating sample magnetometer
XRD	X-ray diffraction
ZFC	Zero-field cooled

ACKNOWLEDGEMENTS

I would like to thank my wife, Amy, who is awesome!

I would also like to thank Professor Ashutosh Tiwari for his continued advice, encouragement, support, and hard work on my behalf. I have really enjoyed learning to be a researcher in the nanostructured materials lab. The opportunity I've had to work here will be a benefit to me for the rest of my life.

Thanks to Mike Scarpulla, Dhananjay Kumar, and Gary Renlund for helpful advice and discussions, and help with some of the experimental procedures and equipment.

CHAPTER 1

INTRODUCTION

Since the advent of integrated circuits (ICs) the semiconductor industry has continued to make major innovations which decrease the size and enhance performance of transistor-based electronics. The trend has closely follow Moore's famous 1965 prediction of doubling the transistor density of an IC every 18 months.[1]

Two major challenges will prevent Moore's trend from continuing indefinitely: First, the scale of current transistor technology is fast approaching the fundamental size limit of single atomic spacings (on the order of 1 nm), and as device dimensions approach this limit quantum effects and current leakage become major problems. Second, heat dissipation also becomes an inhibiting problem due to the inherent nature of charge-based electronics. This is because switching a transistor between the ON and OFF states currently requires moving a charge Q through a channel, requiring a quantity of energy QV where V is the applied voltage. This energy is dissipated as heat after every switching action. One prediction states that if transistor technology continues to progress according to Moore's law, then by 2025 the power dissipation on a single chip will reach 2 MW cm^{-2} (with only a 5% of the transistors active at a given time), a value comparable to the heat dissipation requirement in a rocket nozzle.[2, 3]

1.1 Introduction to Spintronics

Spin transport electronics, or spintronics, has the potential to push transistor technology beyond the Moore era and sidestep the anticipated problems of further miniaturizing charge-only transistor devices. The spintronics approach is to utilize both the charge *and* spin degree of freedom of an electron simultaneously, adding additional functionality to current technology. Since spin is a binary quantity with two possible quantum states in reference to an external field (spin up and spin down) it is an ideal property to use in digital data storage and processing (compared with the fixed scalar charge). The addition of spin functionality will add significant capability and performance enhancements to electronic devices. These advantages include non-volatility (device remembers its state even when unpowered), increased processing speed, decreased power consumption, and higher integration density compared with conventional semiconductor devices.[4]

A number of different applications and devices can be put in the "spintronics" category. Magnetoelectronics are passive spintronics devices, using magnetic or magnetoresistive effects for sensing and storing data.[5] These include giant magnetoresistive (GMR) read-heads for high-density hard disk storage, which have been incorporated into modern iPods, laptops, and desktop computers. Other passive GMR devices include non-volatile magnetic random-access memory (MRAM),[6] programmable spintronic logic devices based on magnetic tunnel junction elements,[7] rotational speed control systems[8] positioning control in robotics and braking systems,[9] magnetometers, and high current monitoring devices for power systems.[10] These devices are all based on sensing how a spin-polarized electric current behaves when it is injected across

ferromagnet-paramagnet interfaces.[5] Active spintronics devices incorporate semiconducting materials for more advanced device applications such as the spin FET (field effect transistor) and spin LED (light emitting diode),[11] as well as spin-only devices like single spin logic (SSL),[12] and ultimately spin-based quantum computing.[13-16]

1.2 Spintronics Applications

1.2.1 GMR and Passive Devices

The discovery of GMR[17, 18] in 1988 led to the development of the spin valve,[19] and eventually merited the 2007 Nobel prize for physics due to its significant impact.[20] The theoretical understanding of how spin valves work is based on the assumption that there are two separate channels of conduction electrons, spin up and spin down, which can behave independently of each other. This two-channel picture, originally proposed by Mott in 1936,[21] explains the behavior of GMR, tunneling magnetoresistance (TMR),[22] and spin injection into metals.[23]

Figure 1.1 shows a simple diagram demonstrating the mechanism of giant magnetoresistance. In a ferromagnetic material the density of states for spin up and spin down states are generally the same, but the energy levels are shifted making the number of available states at the Fermi level different for spin up and spin down polarized charge carriers. This effect is most pronounced in a half metal, as shown in Fig. 1.1, where there the only states at the Fermi energy are from a single spin orientation. When the magnetizations of both ferromagnetic layers are aligned, the resistance is low. When the magnetizations are anti-aligned, the resistance is high since the charge carriers require additional energy to switch spin states before crossing the interface into the second

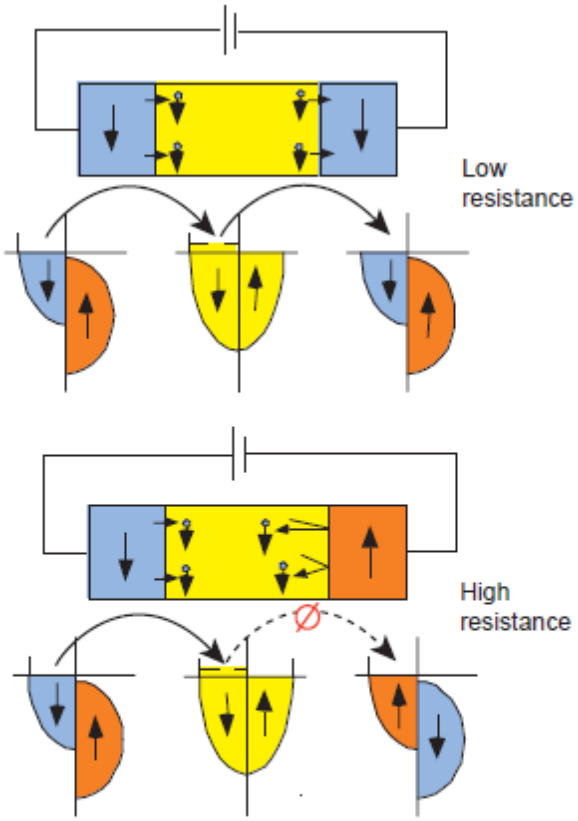

Figure 1.1: Schematic diagram of spin polarized transport through a ferromagnetic metal/ nonmagnetic metal/ ferromagnetic metal for aligned and anti-aligned magnetic moments. From [24]. Reprinted with permission from AAAS.

ferromagnet.[24] Most actual devices do not use the current out-of-plane architecture shown in the figure, but send the current in the plane of the layers, however the resulting high and low resistance states behave the same. It was recently reported that incorporation of GMR technology into magnetic hard-disk storage has already led to a hundredfold increase in storage capacity.[25]

1.2.2 Active devices and semiconductor spintronics

The understanding of device physics for application to active spintronics is progressing along a similar path to what passive spintronics has achieved, making significant progress over the past 10 years.[26] Efforts to create spin-based analogs of conventional transistor devices were catalyzed by Datta and Das's 1990 proposal for the spin-FET.[27] This led to a large effort of experiments and other device proposals, including the spin BJT (bipolar junction transistor).[28, 29] Both of these devices encode information using the charge of the electron (voltages and currents), but spin augments the functionality and improves the performance. In these devices charge current flowing between two terminals is modulated via application of either a voltage or a current at a third terminal. The process by which the voltage or current at the third terminal controls the channel charge is spin-mediated.[30]

1.2.3 The Datta Das Transistor: principles of operation

The Datta Das transistor is almost identical to a conventional FET, but uses an electric field from a typical metal-insulator-semiconductor (MIS) type gate architecture for spin manipulation. The mechanism that allows magnetic spin manipulation using a gate-induced electric field is termed the Rashba spin-orbit (SO) interaction.

A simplified explanation of the Rashba effect is broken down into two well known effects. The Zeeman effect shows how a magnetic field exerts a force on a moving magnetic dipole. Additionally, special relativity tells us that in the rest frame of an electron moving (in the lab frame) through an electric field, there is an effective magnetic field according to the relation:

$$\vec{B} = \frac{\vec{\varepsilon} \times \vec{v}}{c^2} \tag{1.1}$$

In a solid, several other factors must be taken into account to determine the effective magnetic field felt by the electron. Rashba derived the Hamiltonian of a quasi-free electron in a solid taking into account for band-structure, Lande and Thomas correction, and effective mass to find that it is directly proportional to an external electric field: [31]

$$H_{Rashba} = \alpha[\boldsymbol{\sigma} \times \boldsymbol{k}] \tag{1.2}$$

$$\alpha \propto \vec{\varepsilon}(\vec{r}) \tag{1.3}$$

where $\boldsymbol{\sigma}$ is the Pauli spin matrix and $\boldsymbol{k}$ is the momentum vector. The proportionality constant α is the Rashba interaction parameter and is a materials specific property.[5]

The transistor design proposed by Datta and Das consists of three major components as shown in Fig. 1.2. One is the conduction channel, for which they proposed a two-dimensional electron gas (2DEG) formed at the interface of a III-V heterostructure. The second component is a ferromagnetic source and drain, which acts as spin injector (aligner) and detector, respectively. The third component is the MIS electronic gate, which controls current flow through the channel with a gate voltage by manipulating the electron spin in the channel through the aforementioned Rashba interaction.

When the contacts are both magnetically polarized in the same direction, and all scattering mechanisms are ignored, spin current is aligned and flows with low resistance through the entire circuit. This is the ‘on’ state. If the electron spins are flipped within the channel, the current flow into the detector requires another spin flip, and the circuit

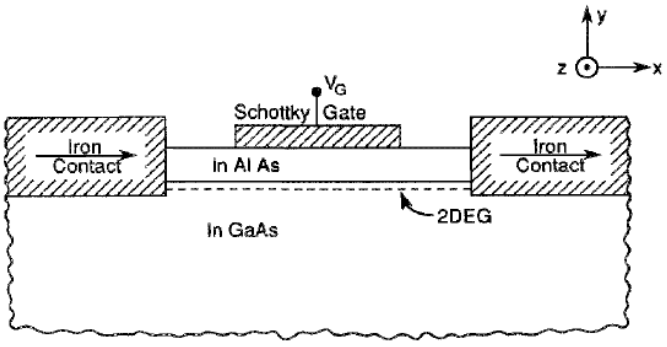

Figure 1.2: Original Das Datta transistor device proposal, later labeled the spin field-effect transistor or SFET. Reprinted with permission from [27]. Copyright 1990, American Institute of Physics.

becomes much more resistive, yielding the 'off' state. The gate applies an electric field which the traveling electrons feel as an effective magnetic field due to the Rashba spin-orbit coupling. This causes the electrons to precess about the field at the Larmor frequency ($f = -egB/2m^*$, e is electron charge, g is the g-factor, B is the magnetic field strength, and m^* is the effective mass) and if the field strength and channel length are sufficient, the degree of rotation could switch the charge polarization from parallel to antiparallel by the time it reaches the detector contact.

1.2.4 Spin Transport in a Semiconductor Channel

Two primary types of spin-orbit interaction are of significance to a quasi-free electron in the conduction band of a semiconductor. The Rashba spin-orbit interaction has been discussed, and is due to an internal electric field inducing an effective magnetic field. The origin of the field can be a built in field at a heterostructure, or an external field, i.e. from a gate voltage. The so-called Dresselhaus interaction is another mechanism which causes precession of spins in semiconductors lacking crystallographic inversion asymmetry (compound semiconductors).

Three mechanisms of spin scattering are known to occur within the spin channel, and must be considered in spin transport devices. The Elliot-Yafet (EY) mechanism is a spin-flip event due to a momentum change resulting from a carrier collision with an impurity or phonon.[32, 33] For this reason low temperatures and high-quality crystals decrease the EY scattering mechanism contribution. EY is usually the dominant scattering mechanism in metals and low-bandgap semiconductors.[5] D'yakonov-Perel (DP) spin scattering is usually the dominant scattering mechanism in high quality semiconductor crystals. It can be thought of as unwanted spin relaxation by the Rashba and Dresselhaus spin-orbit interaction from fluctuating effective magnetic fields due to momentum scattering.[34] Therefore the same spin-orbit interaction parameters which enhance the gate-voltage induced effective field in a spin-FET can reduce the spin coherence time. For this reason, material optimization must be performed so that the SO interaction is sufficient that spin can be controlled with a gate induced field, but not so high that unwanted spin relaxation reduces the spin diffusion length below the channel length from DP scattering. The third spin scattering mechanism of note is the Bir-Aronov-Pikus (BAP) mechanism. This mechanism results from interaction of negative and positive charge carriers, and so can be neglected in materials without both a high electron and hole concentration.[35] These three relaxation mechanisms are the main factors that reduce spin coherence lengths in spin transistor devices, and so should be minimized to achieve the best performance.

1.2.5 Spin Injection into Semiconductors

There has not yet been a successfully realized spin FET device, despite considerable experimental effort. Gate voltage control of the Rashba interaction has been experimentally demonstrated, but not to the degree needed for detectable modulation of the source-drain current.[36] The primary obstacle inhibiting the experimental demonstration of a Datta-Das or similar spin FET is poor spin injection and detection efficiencies at the source/channel and drain/channel interfaces.[3] This is because if either the source or drain efficiency is below 100%, then electrons with the wrong spin polarization will degrade the ON/OFF conductance ratio. The maximum conductance ratio in a spin FET is given by: [5, 37]

$$\eta = \frac{I_{ON}}{I_{OFF}} = \frac{1+\xi_S\xi_D}{1-\xi_S\xi_D} \tag{1.4}$$

where ξ_S and ξ_D are the source injection and drain detection efficiencies, respectively. The ON/OFF ratio is infinity when $\xi_S = \xi_D = 1$, but falls off rapidly with decreasing efficiencies. Small injection and detection efficiencies also allow leakage current during the OFF state, which can lead to device errors.

There has been significant research effort and progress towards improving spin injection and detection efficiencies in the past ten years. The closer these efficiencies come to 100%, the closer we will be to implementing viable spintronic devices into modern technology. Initially ferromagnetic metals such as permalloy ($Ni_{80}Fe_{20}$) were used for spin injection of polarized carriers directly into a semiconducting channel.[38, 39] This method, however, yielded an injection efficiency of less than 1% due to significant spin-flip scattering at the highly impedence-mismatched interface.[40] To improve on this efficiency three different methods have been proposed and employed: First, tunneling of

spin polarized carriers from ferromagnetic metals through an insulating barrier[41]; second, tunneling from a nonmagnetic metal contact through a ferromagnetic insulating barrier, which acts as a spin filter[42-44]; third, injection of spin polarized carriers from a dilute magnetic semiconductor into a conventional semiconductor.[45] In the first two methods the tunneling process is spin conservative, so the scattering from impedance mismatch is avoided and very high efficiencies can be achieved. In the third method the conductivity of the two semiconductors can be closely matched to minimize spin-flip scattering at the interface.

Using the first method, initial reports were around 30% room temperature spin injection efficiency[41] in 2002, which was quickly increased to 70% spin injection efficiency in 2005, using an MgO tunnel barrier and GaAs semiconductor.[46] Improvements in epitaxial growth techniques for high quality tunnel barriers are expected to continue to raise this number, meaning tunneling injection may be a viable option for actual device implementation very soon. This preliminary research motivates chapters five and six in the present work.

Early work using the second method showed 85% injection efficiency at low temperatures[42] in EuS. This report, along with the success in the field of dilute magnetic semiconductors, led to an effort to engineer new materials which were simultaneously ferromagnetic and electrically insulating, called dilute magnetic dielectrics (DMD). In 2001 room temperature ferromagnetism was reported in Co doped TiO_2,[47] a high dielectric constant material with a very wide bandgap. After this initial report several other groups confirmed observation of ferromagnetism in both rutile[48] and anatase[49, 50] phase Co:TiO_2. Subsequent research demonstrated room temperature ferromagnetism in

other insulating materials such as Fe-doped SnO_2,[51] Mn-doped GaN,[52] and Co-doped CeO_2.[53] Most of the research has focused on materials engineering of these dilute magnetic dielectrics to achieve optimal room temperature magnetic properties, and understand the physics of the exchange mechanism responsible for the ferromagnetic response.

1.3 Objectives

Recent advances in the field of spintronics have motivated the present work in two major ways. First, as described in Chapters 3-4, the engineering of new magnetic insulators for spin tunnel injection applications was the primary goal of our initial research into the rare earth oxide compounds Sm_2O_3 and Tb_2O_3.

The objectives of our Sm_2O_3 research are described as follows:

(1) Synthesis and characterization of new DMD material based on the samarium oxide system.

(2) Analysis of magnetic behavior to gain insight into the exchange mechanism and correlate the material morphology and other properties to the magnetic response.

In the case of terbium oxide, thin films of the material were not as well studied or developed, so the initial objectives were preliminary to synthesis of another new DMD.

(1) Synthesis and characterization of terbium oxide thin films on various substrates. Preliminary investigation of crystal growth, morphology, and electrical properties in preparation for magnetic doping.

(2) Viability of Tb_2O_3 as a high-k dielectric material for complementary metal oxide semiconductor (CMOS) applications is also explored.

Chapters 5-6 comprise our investigation of conventional tunnel barriers to characterize spin transport in two technologically important semiconductor materials. The objectives of these studies are as follows:

(1) Demonstrate spin injection and detection using all-electrical means in Si using MgO based tunnel barrier. Compare spin transport with published results using similar Al_2O_3 barrier.

(2) Demonstrate spin injection and detection using all-electrical means in ZnO using MgO based tunnel barrier. Determine spin life-time using this configuration.

1.4 References

1. G. Moore, Electronics Magazine **38** iss. 8, April 19, 1965

2. The International Technology Roadmap for Semiconductors, available at http://www.itrs.net.

3. S. Bandyopadhyay and M. Cahay, Nanotechnology **20**, 412001 (2009).

4. S. A. Wolf, D. D. Awschalom, R. A. Buhrman, J. M. Daughton, S. von Molnar, M. L. Roukes, A. Y. Chtchelkanova, and D. M. Treger, Science **294**, 1488 (2001).

5. S. Bandyopadhyay and M. Cahay, *Introduction to Spintronics* (CRC Press, Boca Raton, FL, 2008).

6. P. P. Freitas, F. Silva, N. J. Oliveira, L. V. Melo, L. Costa, and N. Almeida, Sensors and Actuators A: Physical **81**, 2 (2000).

7. J. Wang, H. Meng, and J. Wang, J. Appl. Phys. **97**, 10D509 (2005).

8. P. Freitas, J. Costa, N. Almeida, L. Melo, F. Silva, J. Bernardo, and C. Santos, J. Appl. Phys. **85**, 5459 (1999).

9. W. Ku, P. P. Freitas, P. Compadrinho, and J. Barata, Magnetics, IEEE Transactions on **36**, 2782 (2000).

10. J. Pelegri, J. B. Ejea, D. Ramirez, and P. P. Freitas, Sensors and Actuators A: Physical **105**, 132 (2003).

11. M. Holub and P. Bhattacharya, J. Phys. D: **40**, R179 (2007).

12. S. Bandyopadhyay, B. Das, and A. E. Miller, Nanotechnology **5**, 113 (1994).

13. A. Bychkov, L. Openov, and I. Semenihin, JETP Letters **66**, 298 (1997).

14. D. Loss and D. P. DiVincenzo, Physical Review A **57**, 120 (1998).

15. S. Bandyopadhyay, Phys. Rev. B: **61**, 13813 (2000).

16. B. E. Kane, Nature **393**, 133 (1998).

17. M. N. Baibich, J. M. Broto, A. Fert, F. N. Van Dau, F. Petroff, P. Etienne, G. Creuzet, A. Friederich, and J. Chazelas, Phys. Rev. Lett. **61**, 2472 (1988).

18. G. Binasch, P. Grunberg, F. Saurenbach, and W. Zinn, Phys. Rev. B: **39**, 4828 (1989).

19. B. Dieny, V. S. Speriosu, S. S. P. Parkin, B. A. Gurney, D. R. Wilhoit, and D. Mauri, Phys. Rev. B: **43**, 1297 (1991).

20. A. Fert, Rev. Mod. Phys. **80**, 1517 (2008).

21. N. F. Mott, Proc. R. Soc. Lond. A **153**, 699 (1936).

22. J. S. Moodera, L. R. Kinder, T. M. Wong, and R. Meservey, Phys. Rev. Lett. **74**, 3273 (1995).

23. M. Johnson and R. H. Silsbee, Phys. Rev. B: **37**, 5326 (1988).

24. G. A. Prinz, Science **282**, 1660 (1998).

25. J. Fabian, A. Matos-Abiague, C. Ertler, P. Stano, and I. Zutic, Acta Physica Slovaca **57**, 565 (2007).

26. D. D. Awschalom and M. E. Flatte, Nature Phys. **3**, 153 (2007).

27. S. Datta and B. Das, Appl. Phys. Lett. **56**, 665 (1990).

28. J. Fabian, I. Zutic, and S. Das Sarma, Appl. Phys. Lett. **84**, 85 (2004).

29. M. Flatté and G. Vignale, Appl. Phys. Lett. **78**, 1273 (2001).

30. S. Bandyopadhyay and M. Cahay, Appl. Phys. Lett. **85**, 1814 (2004).

31. E. Rashba, Sov. Phys. Solid State **2**, 1109 (1960).

32. R. J. Elliott, Phys. Rev. **96**, 266 (1954).

33. Y. Yafet, *Solid State Physics* (Academic, New York, 1963).

34. M. D'yakonov and V. Perel, Sov. Phys. Solid State **13**, 3023 (1972).

35. I. Zutic, J. Fabian, and S. Das Sarma, Rev. Mod. Phys. **76**, 323 (2004).

36. J. Nitta, T. Akazaki, H. Takayanagi, and T. Enoki, Phys. Rev. Lett. **78**, 1335 (1997).

37. A. Trivedi, S. Bandyopadhyay, and M. Cahay, IET Circuits, Devices Syst. **1**, 395 (2007).

38. W. Lee, S. Gardelis, B. Choi, Y. Xu, C. Smith, C. Barnes, D. Ritchie, E. Linfield, and J. Bland, J. Appl. Phys. **85**, 6682 (1999).

39. P. R. Hammar, B. R. Bennett, M. J. Yang, and M. Johnson, Phys. Rev. Lett. **83**, 203 (1999).

40. G. Schmidt, D. Ferrand, L. W. Molenkamp, A. T. Filip, and B. J. van Wees, Phys. Rev. B: **62**, R4790 (2000).

41. A. Hanbicki, B. Jonker, G. Itskos, G. Kioseoglou, and A. Petrou, Appl. Phys. Lett. **80**, 1240 (2002).

42. X. Hao, J. S. Moodera, and R. Meservey, Phys. Rev. B: **42**, 8235 (1990).

43. I. V. Shvets, A. N. Grigorenko, K. S. Novoselov, and D. J. Mapps, Appl. Phys. Lett. **86**, 212501 (2005).

44. R. Fiederling, M. Keim, G. Reuscher, W. Ossau, G. Schmidt, A. Waag, and L. W. Molenkamp, Nature **402**, 787 (1999).

45. S. J. Pearton, W. H. Heo, M. Ivill, D. P. Norton, and T. Steiner, Semiconductor Science and Technology **19**, R59 (2004).

46. G. Salis, R. Wang, X. Jiang, R. M. Shelby, S. S. Parkin, S. R. Bank, and J. S. Harris, Appl. Phys. Lett. **87**, 262503 (2005).

47. Y. Matsumoto, et al., Science **291**, 854 (2001).

48. Y. Matsumoto, et al., Jpn. J. Appl. Phys. **40**, L1204 (2001).

49. S. Chambers, et al., Appl. Phys. Lett. **79**, 3467 (2001).

50. K. A. Griffin, A. B. Pakhomov, C. M. Wang, S. M. Heald, and K. M. Krishnan, Phys. Rev. Lett. **94**, 157204 (2005).

51. J. Coey, Appl. Phys. Lett. **84**, 1332 (2004).

52. T. Sasaki, S. Sonoda, Y. Yamamoto, K.-i. Suga, S. Shimizu, K. Kindo, and H. Hori, J. Appl. Phys. **91**, 7911 (2002).

53. A. Tiwari, V. M. Bhosle, S. Ramachandran, N. Sudhakar, J. Narayan, S. Budak, and A. Gupta, Appl. Phys. Lett. **88**, 142511 (2006).

CHAPTER 2

BACKGROUND AND EXPERIMENTAL TECHNIQUES

2.1 Processing

The majority of thin films produced for this study were deposited using pulsed laser deposition (PLD). Targets were produced from powders using ceramic processing to produce one-inch diameter disks. A sol-gel processing technique was used to create the powder precursor of Co doped Sm_2O_3.

Additional thin film processing techniques for device fabrication included photolithography, atomic layer deposition (ALD), and electron-beam assisted evaporation.

2.1.1 Bulk Target Processing: Sol-gel

Sol-gel is a wet-chemical technique commonly used to fabricate materials by into a gel network or discrete nanoparticles from a colloidal suspensions or solutions (sol).[1] We used a citrate sol-gel process to make $Sm_{2-x}Co_xO_3$ powders. This is a low temperature, rapid process capable of making homogeneous, single phase metal oxide powders even if solvent ratios are higher than the solubility limit for conventional solid-

state processing. Precursors to the desired materials, such as metal salts (we typically used nitrates) and oxides are dissolved and mixed into a single solution in precise stoichiometric ratios.

For $Sm_{2-x}Co_xO_3$, commercially available Sm_2O_3 was dissolved in concentrated nitric acid, and $Co(NO_3)_2*6H_2O$ was dissolved in water as a Co precursor. A flow-chart of the sol-gel process used is shown in Fig. 2.1. Citric acid ($C_6H_8O_7$) was dissolved in water and added to the metal ion solution in a 1:1 molecular ratio. Citric acid was used as a chelating agent. Solutions were refluxed at 100 °C for 12 hours to create metal citrates through the following reactions:

$$C_6H_5O_7H_3 \rightarrow (C_6H_5O_7)^{3-} + 3H^+, \text{ in water}$$

$$(C_6H_5O_7)^{3-} + M^{n+} \rightarrow (C_6H_5O_7)_nM_3$$

In the first reaction citric acid dissociates in water to form a $(C_6H_5O_7)^{3-}$ ion. When combined with a solution containing metal ions (M^{n+}) of oxidation state *n* metal citrates are formed.[2]

After the reflux step, the condenser apparatus is removed and the solution heated to evaporate the water. When the water is nearly gone, the citrate chains begin to polymerize, and a gel forms. Continued heating results in an exothermic reaction at around 160° C resulting in a nanostructured network, which was ground to make a powder. The resulting powder is then placed in a furnace and the remaining carbon is burned out at 1000° C for 12 hours.

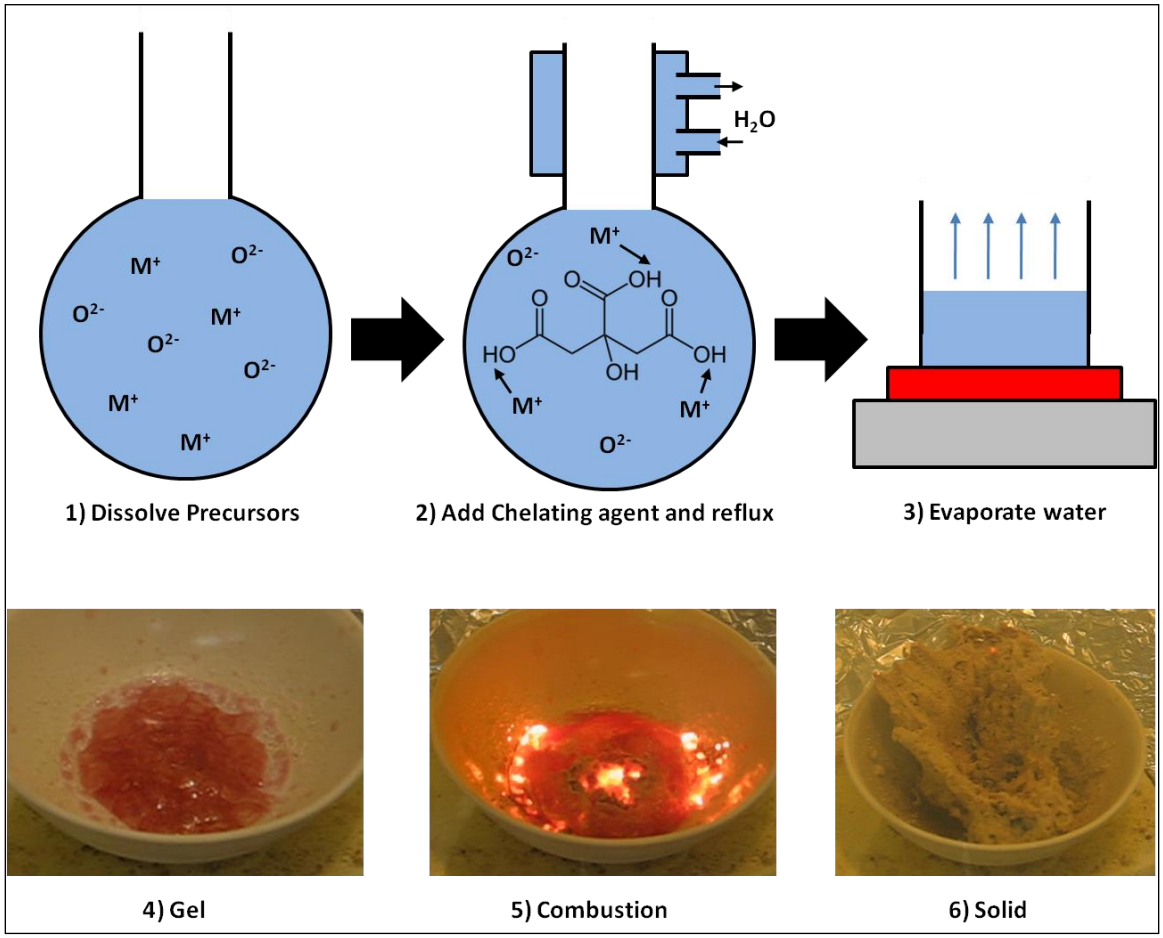

Figure 2.1. Schematic flow diagram of the sol-gel process. Images taken from $Sm_{2-x}Co_xO_3$ sol-gel sample.

The resulting powders were pressed using a biaxial press under 200MPa of pressure with a 1" die. The 1" pellets were sintered at approximately 80% of the melting temperature of the material to make densified ceramic targets for PLD ablation. The resulting targets were characterized using x-ray diffraction and energy-dispersive x-ray specroscopy to determine phase and chemical composition.

2.1.2 Pulsed Laser Deposition

In pulsed laser deposition (PLD) a high-powered pulsed excimer laser is used to ablate material from the surface of a solid target and deposit thin films on a substrate. PLD can provide very high quality epitaxial films under the right conditions when using single crystal substrates. The PLD technique maintains stoichiometry of the material as it is transferred from the target to the substrate, and is very versatile in the types of targets which can be used.

The laser typically delivers energy densities from 1-5 J/cm^2 to the target in each 25 nanosecond pulse, delivering a power density of 1 GW/cm^2. The target region absorbing the laser power can reach localized temperatures as high as 25,000 K.[3] This produces a plasma plume directed normal away from the surface of the target. The plume expands accelerating the ablated plasma forward where the plasma condenses on a comparatively cool substrate. These extremely high temperatures enable the stoichiometric transfer of target material. The thermal energy in the plasma is converted to kinetic energy as the plume expandes. Due to the high kinetic energy of material condensed on the substrate surface, the PLD technique requires lower epitaxial growth temperatures than other techniques. Figure 2.2 shows a diagram of our PLD system.

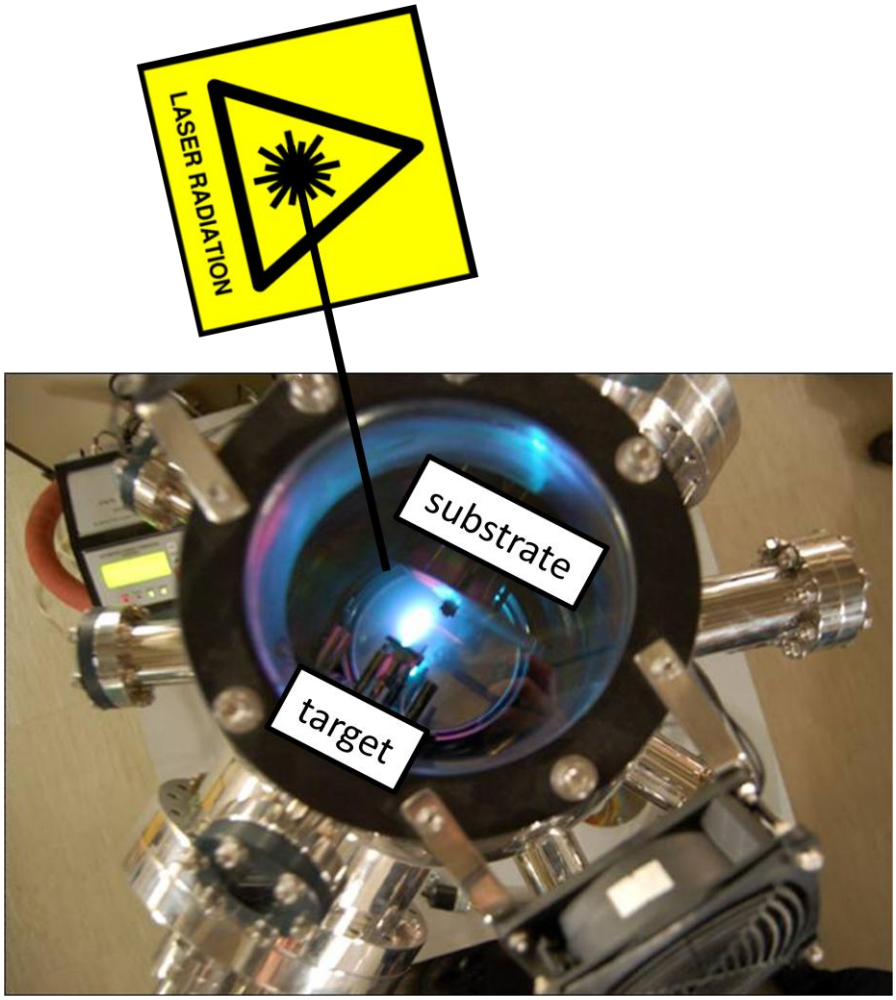

Figure 2.2. Our pulsed laser deposition (PLD) system uses a 248 nm KrF laser ablates a ceramic target with 25 ns pulses. The resulting plasma condenses on a heated substrate, depositing a highly crystalline thin film.

All of the thin films deposited by PLD in this work were ablated from ceramic targets using a Compex Pro 205 KrF excimer laser. The wavelength is 248 nm, with a 25 ns pulse. The targets were mounted on a carousel in a high vacuum chamber which could also be backfilled with oxygen gas, and rotated at 3 Hz to ensure that nonlocal heating did not induce melting of the target during the depositions. The substrate was mounted on a heater using silver paint, and when necessary shadow masks were used to achieve

needed device geometries. Other works have shown that in films deposited by PLD the film stoichiometry closely matches the target stoichiometry,[3] so all films presented are assumed to have the same composition as the target, with a homogeneous distribution of elements.

2.1.3 Atomic Layer Deposition (ALD)

Atomic layer deposition was used to make very thin layers of Al_2O_3 film for use as tunnel barriers as outlined in Chapter 5 of this work. ALD was chosen because of its reliability in making very thin films free of pinholes or other unwanted features, which is a necessary requirement for tunneling.

This technique is a highly controlled chemical vapor deposition method. Two precursors are used sequentially, resulting in growth of compounds a single layer at a time.

For Al_2O_3 deposition, trimethyl-aluminum (TMA) gas is first injected into the vacuum chamber exposing the substrate. The TMA reacts with a single layer coating of hydroxyl groups (i.e, Si-O-H) present on the substrate surface. These have formed from H_2O vapor in air adsorbed on the substrate before it was loaded into the vacuum. At the film surface this gas reacts with the adsorbed Al precursor to form a single atomic layer of Al_2O_3 and methane gas, according to:[4]

$$Al(CH_3)_{3(g)} + :Si\text{-}O\text{-}H_{(s)} \rightarrow :Si\text{-}O\text{-}Al(CH_3)_{2(s)} + CH_4$$

The methyl groups cannot react with themselves, so the reaction terminates after the substrate is coated with only a single atomic layer of Al. The remaining unreacted TMA and product methane gas is purged from the chamber. This step is illustrated in

Fig. 2.3a.

Second, H_2O gas is injected. At the film surface the H_2O reacts with the dangling methyl groups, forming methane gas and replace the methyl with hydroxyl groups as shown in Fig. 2.3b:

$$2\ H_2O + Si\text{-}O\text{-}Al(CH_3)_{2(s)} \rightarrow :Si\text{-}O\text{-}Al(OH)_{2(s)} + 2CH_4$$

The methane and remaining H_2O are then purged from the system and the cycle is repeated until the desired thickness is reached. This slow process has the advantage of highly uniform films with precise control over thickness.

For our tunnel barriers a Cambridge Nanotech Fiji F200 ALD was used, with substrate heated to 250 °C.

2.1.4 Electron-beam Assisted Thermal Evaporation

The electron-beam assisted thermal evaporation (e-beam) technique was used to deposit top electrodes on the tunnel barrier contact devices reported in this work. This technique was used over PLD or other available techniques because of the requirement that the metal cannot penetrate or diffuse through the extremely thin (<1nm) tunnel barrier at any point. Material deposited by e-beam evaporation has relatively low kinetic energy when it condenses on the substrate, and so will not penetrate then tunnel barrier by forming short circuit pathways which would bypass the tunneling mechanism. this is a fairly straightforward technique, in which the desired material (in our case $Ni_{80}Fe_{20}$ metal) is placed in a graphite crucible and loaded into a high vacuum chamber. The target metal is heated by means of a high-voltage electron beam, which oscillates accross the surface heating to the melting temperature. Once melted, a shutter is opened allowing

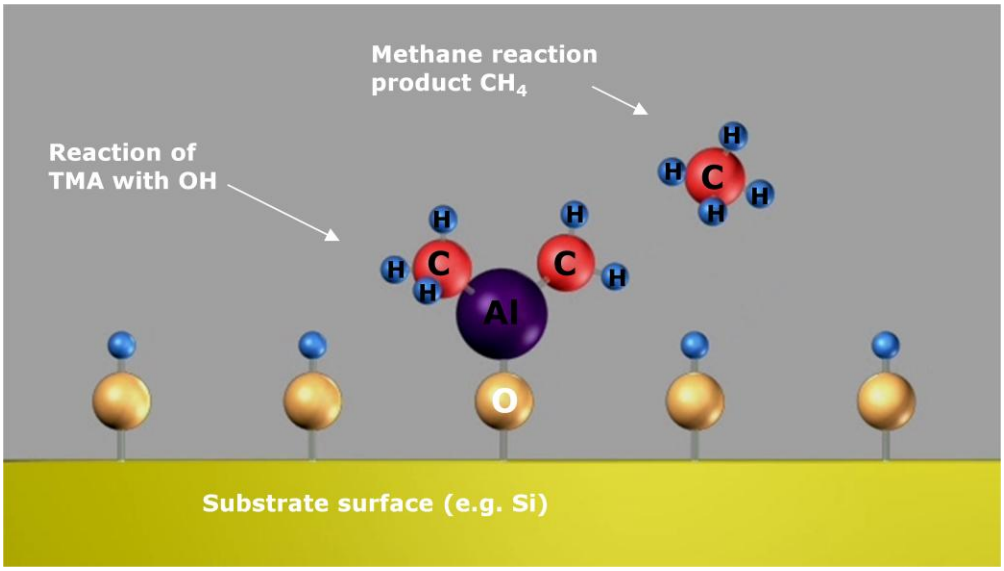

$$Al(CH_3)_{3\,(g)} + :Si\text{-}O\text{-}H_{\,(s)} \longrightarrow :Si\text{-}O\text{-}Al(CH_3)_{2\,(s)} + CH_4$$

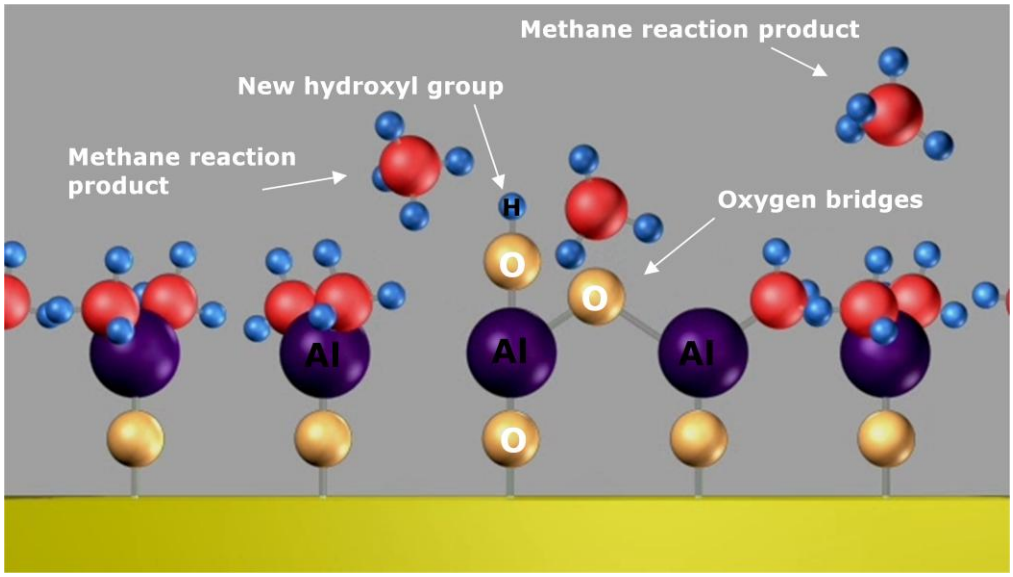

$$2\,H_2O_{\,(g)} + :Si\text{-}O\text{-}Al(CH_3)_{2\,(s)} \qquad :Si\text{-}O\text{-}Al(OH)_{2\,(s)} + 2\,CH_4$$

Figure. 2.3: Diagram showing growth mechanism of Al_2O_3 in the atomic layer depositions (ALD) technique. (a) Trimethylaluminum (TMA) reacts with the adsorbed hydroxyl groups, producing methane as the reaction product. (b) H_2O reacts with the dangling methyl groups on the new surface forming aluminum-oxygen (Al-O) bridges and hydroxyl surface groups, waiting for a new TMA pulse. Again methane is the reaction product. From [4]. Reprinted with permission from Cambridge Nanotech Inc.

the evaporating material to condense on the substrate surface. An Inficon crystal thickness monitor can be used to ensure the film has the correct thickness.

Our films were deposited using a Denton SJ20C e-beam evaporator and were all 20nm thick. The Ni/Fe ratio is not perfectly conserved in this process due to differing melt temperatures, but the resultant films still met our requirements.

2.1.5 Optical Photolithography

Optical photolithography is a staple technique in the semiconductor industry. It involves transferring the pattern from a mask onto a light-sensitive chemical coating "photoresist" in order to selectively remove portions of a thin film for electronic devices. The photolithography process used in the present work was used in a number of processing steps, including selective channel etching of SiO_2 and growth of a specific geometry of isolated top metal contacts. To ensure reproducibility of all reported values the complete photolithography recipe is reported:

Shipley 1813 photoresist was spin-coated onto the substrate at 2000 rpm for 1 minute. The entire substrate was heated to 110 °C for 1 minute to set the resist. The mask was a chrome coated glass plate, with the chrome removed where the photoresist was to be exposed by an "electromask" pattern generator. The photoresist was exposed to the OAI 206 Mask Aligner UV lamp for 8 seconds, and then developed in 352 developer for ~45 seconds. After desired processing was complete, the remaining resist was stripped by ultrasonicating in acetone.

2.2 Characterization

2.2.1 X-ray Diffraction

X-ray diffraction (XRD) was used to determine the crystal phase(s) and orientation relationship to substrate for the thin films studied. The primary diffractometer used for θ-2θ scan XRD was a Phillips X'pert with Cu source element producing a strong 1.54Å x-ray line. Bragg reflections from a crystal give strong signals at angles corresponding to the out-of-plane lattice plane spacing according to Bragg's law: $n\lambda=2d\ sin\theta$. In order to determine in-plane orientation relationship between film and substrate a Bruker D8 diffractometer with monochromator and azimuthal Φ-scan rotation was used. The sample was fixed at a single θ angle, and rotated in the Φ direction 360° to determine how many in-plane crystallographic orientations there are. For cubic crystals with a single orientation (epitaxial), a Φ-scan will give a symmetric pattern of four peaks.

2.2.2 Transmission Electron Microscopy

The transmission electron microscope (TEM) is a state-of-the-art imaging tool with the highest resolution currently available for microstructural analysis. In a TEM high energy electrons (200-300 keV) are generated from a field emission gun in a high vacuum chamber. The electrons are accelerated through a series of electromagnetic lenses onto a very thin (<100nm) sample. A number of techniques can be performed to collect and analyze the transmitted electrons. A Tecnai F30 300kV TEM was used to image cross sections of thin films and interfaces in this work. The primary image methods used were diffraction contrast mode (bright and dark field) and phase contrast mode for high resolution or HRTEM. Diffraction contrast mode measures the intensity

of electron diffraction across the sample, and is useful for imaging defects such as dislocations, interfaces, and second phase particles. Phase contrast mode HRTEM preserves the phase of the diffracted electrons which interfere constructively or destructively with the transmitted beam to form images of columns of atoms.[5] Electron diffraction was also used to compliment x-ray diffraction, with the advantage of being able to focus the electron beam on a specific selected area and get local diffraction information. These techniques were all used to examine orientation relationships, defects and grain boundaries, film thickness, and to search for the presence of secondary phases.

2.2.3 Scanning Electron Microscopy and Energy Dispersive X-ray Spectroscopy

Scanning electron microscopy (SEM) was used to examine PLD targets and deposited thin films and deposited devices. A Hitachi S3000-N SEM using the secondary electron detector was used to analyze film surfaces. Energy dispersive x-ray spectroscopy (EDS) was used for elemental and compositional analysis of thin films and targets. The Hitachi S3000-N is equipped with an EDX liquid nitrogen cooled sapphire detector. In EDS incident electrons displace inner shell electron of an atom in a sample. Outer shell electrons relax into the vacant inner shell producing an x-ray, which is characteristic of each element.

2.2.4 SQUID Magnetization Measurement

Magnetic measurements for thin films were performed in collaboration with D. Kumar at North Carolina A&T State University using a Quantum Design vibrating

sample magnetometer (VSM) with a superconducting quantum interference device (SQUID) detector. In this measurement an applied field (H) is generated up using a superconducting magnet, and the magnetization of the sample (M) is measured by moving a sample through the SQUID detector inducing a current. The measured current is proportional to the magnetic flux through the detector.

2.2.5 Ultra Violet/Visible Transmission Spectroscopy

Ultra Violet/ Visible (UV/Vis) transmission spectroscopy was used to measure the band gap and wavelength dependent absorption of thin films. A Shimadzu model 1240 UV/Visible scanning spectrophotometer was used to scan wavelengths from 190-1100 nm and the substrate spectrum was used as a baseline. The transmission data (T) measure the normalized intensity I/I_0 across the wavelength range. The bandgap can be extracted by fitting the absorption edge to the Tauc equation:[6]

$$\alpha = C(h\nu - E_g)^n \tag{2.1}$$

where absorbance (α) is α = -log(T), C is a constant, $h\nu$ is photon energy in eV, and n is ½ for direct band gap material and 2 for an indirect band gap material.

2.2.6 Dielectric Constant Measurements

The dielectric constant k is a measure of the capacitance of a material compared with free space. By measuring capacitance the dielectric constant is computed according to $k = C\,d/\varepsilon_0 A$, where C is capacitance, d is thickness, ε_0 is the permittivity of free space, and A is the contact area. An accurate measure of the true dielectric constant of a

material can be difficult to make due to parasitic impedence contributions in the measurement system, connection wires, contacts, and even in the sample. In order to ensure the most accurate measurement possible, a probe station test fixture was used, with voltage and current signals separated into four shielded coaxial cable leads. AC measurements were performed in a range of frequencies up to 6 MHz to ensure that no significant change in capacitance was observed, and dielectric loss D was minimized. Two different test apparatus were used, a Gamry Instruments Reference 600 potentiostat up to 6 MHz, and an HP 4284A precision LCR meter, and agreement between values taken on both different machines indicated accuracy in the mesaurement setup.

2.2.7 Three-Terminal Hanle Effect

The three-terminal Hanle effect was used to determine the spin coherence time τ_s of charge carriers in semiconductor materials. This technique is described in greater detail in Chapter 5. The purpose is to measure the resistance of a single magnetic junction by isolating the spin accumulation voltage V_S.

Spin polarized current is first injected into a semiconducting channel as shown in Fig. 2.4a, causing a spin-dependent imbalance in the electron population of the conduction band. At steady state conditions, the imbalance is compensated for by a difference in the electrochemical potentials for spin up and spin down charge carriers, designated $\mu\uparrow$ and $\mu\downarrow$. The resulting accumulation $\Delta\mu=\mu\uparrow-\mu\downarrow$ is directly proportional to the spin voltage V_s. When a transverse magnetic field B is applied, the spins of the carriers precess about the field at the Larmour frequency $\omega_L = 2\pi g\mu_B/h$. The Larmor precession randomizes the spins as shown in Fig. 2.4b, quenching $\Delta\mu$, corresponding to a

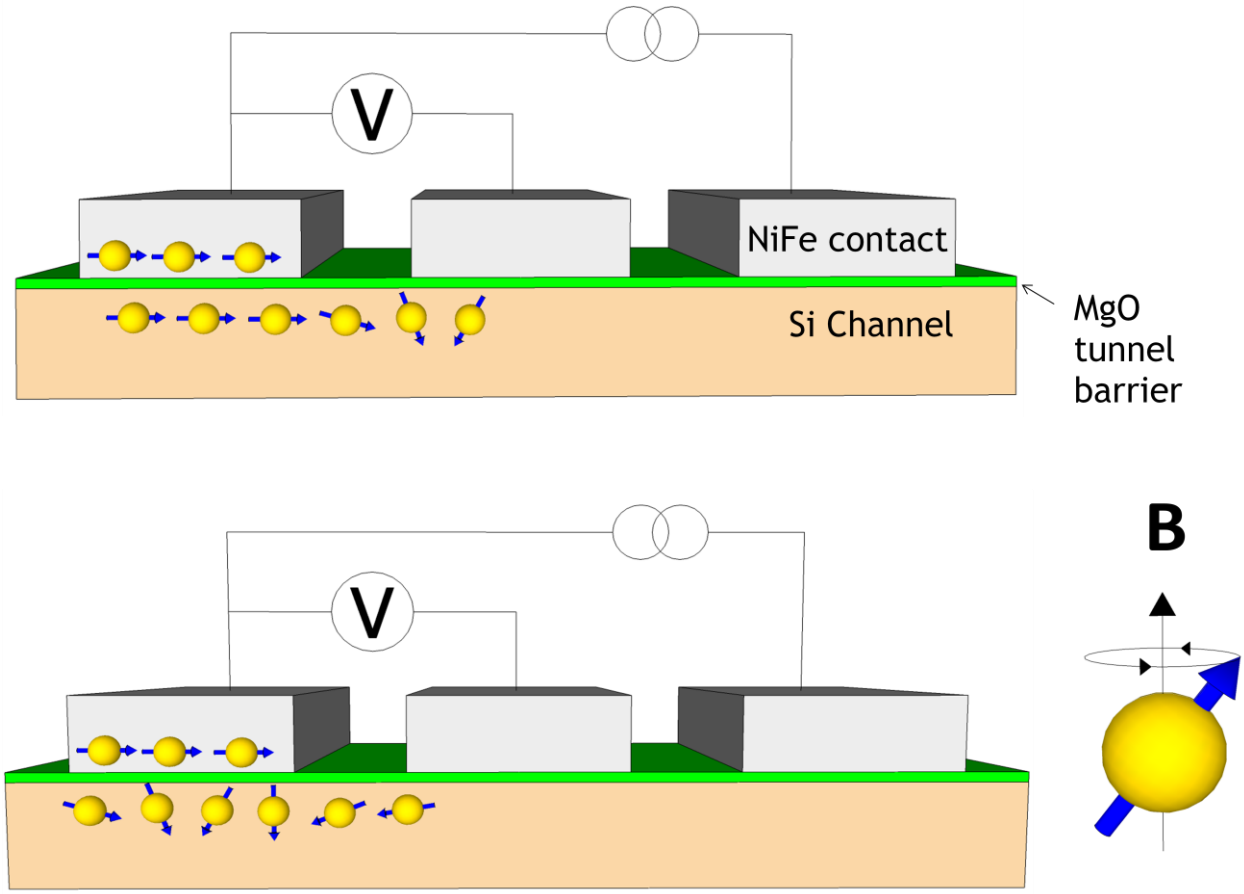

Figure 2.4: A tunneling spin injection device in three-terminal Hanle geometry. The ferromagnetic metal terminal injects a spin polarized current into the channel. The spins retain their polarization in the channel for a lifetime τ_s. (a) This results in the accumulation of spin directly beneath the probe (left) contact. The other two contacts are used as voltage and current references. (b) When a transverse magnetic field is applied, the spin accumulation is eliminated in the semiconductor channel due to Larmour precession of electron spins about the field.

reduction in the voltage signal V_s according to the electrical Hanle equation:

$$V_S = TSP \times \frac{\Delta\mu(0)}{2(1+(\omega_L\tau)^2)} \quad (2.2)$$

where TSP is the tunnel spin polarization of the contact.[7]

These measurements were taken in a closed cycle helium refrigerator so that temperature could be precisely controlled (Fig. 2.5).

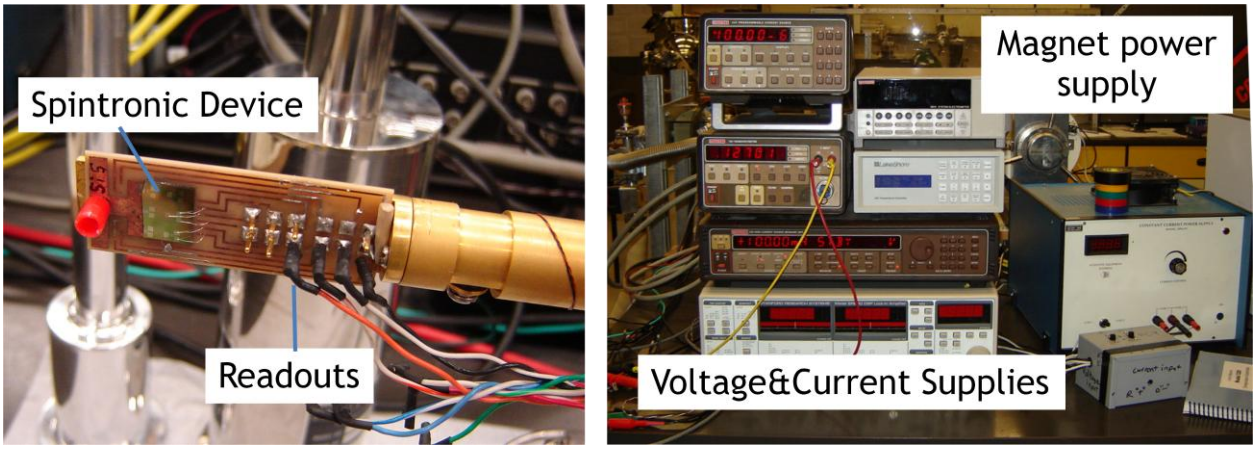

Figure 2.5 Experimental set-up used for three-terminal Hanle measurements. Devices were mounted and wired to a test circuit (left) and cooled with a closed cycle He refrigerator. All electronic controls and power supplies (right) were linked and operated via labview.

2.3 References

1. P. Gao, Y. Ding, W. Mai, W. Hughes, C. Lao, and Z. Wang, Science **309**, (2005).

2. C. J. Brinker and G. W. Scherer, *Sol-Gel Science*, (Academic Press inc., San Diego, 1990).

3. R. Singh and J. Narayan, Phys. Rev. B **41**, 8843 (1990).

4. http://www.slideshare.net/CambridgeNano/ald-tutorial-8818400

5. B. Fultz and J. M. Howe, *Transmission Electron Microscopy and Diffractometry of Materials* (Springer press, Germany, 2008).

6. *Semiconductors and Semimetals*, edited by R. K. Willardson and A. C. Beer (Academic, New York, 1967).

7. S. P. Dash, S. Sharma, R. S. Patel, M. P. de Jong, and R. Jansen, Nature **462**, 491 (2009).

CHAPTER 3

DYNAMIC SUPERPARAMAGNETISM IN PRECIPITATE FREE $Sm_{1.9}Co_{0.1}O_3$ THIN FILMS

3.1 Abstract

This chapter reports Samarium Oxide (Sm_2O_3) doped with a small amount of cobalt (Co) is shown to exhibit a magnetic phenomenon which cannot be accounted for by conventional models. Though the observed magnetic properties appear quite similar to those observed in superparamagnetic systems, the origin of these properties is entirely different. Careful microstructural analysis showed no secondary phases or compositional variation which could account for the observed magnetic response. A model, based on the widely accepted bound polaron theory for insulating ferromagnets, is proposed to explain the magnetic behavior of Co doped Sm_2O_3 films. In this model, exchange mediating defects form magnetically active regions that behave like superparamagnetic clusters; however, unlike superparamagnetic systems the size of magnetically active regions is not static but changes dynamically with temperature.

3.2 Introduction

It is widely believed that the successful integration of spin functionality into present CMOS based electronic devices will improve their processing speed, storage capacity and power requirement.[1, 2] The above notion has led to the discovery of several new and exotic materials which in many cases exhibit phenomena that cannot be adequately explained by current physical models. One such example is the discovery of dilute magnetic dielectrics (DMD). Specifically a number of highly insulating oxides such as TiO_2 (anatase),[3] HfO_2,[4, 5] GaN,[6, 7] SnO_2[8] and CeO_2[9, 10] have been reported to show room temperature ferromagnetism when doped with small amounts of transition metal elements. Such systems exhibit ferromagnetic long range ordering even though the magnetic dopant level is far below the percolation limit[11] for dipole exchange interaction. In these insulating systems, carrier mediated RKKY magnetic exchange cannot be applied to explain the observed ferromagnetism, and other mechanisms such as super-exchange or double exchange also fall short.[12]

In order for spintronics to become a reality in the near future, we must develop a better understanding of the origin of ferromagnetism in spintronic materials. Recently Coey *et al.*[12] outlined a defect-mediated mechanism which accounts for the observed ferromagnetic behavior of DMDs. In this model electrons bound by defects form hydrogen-like "polarons." When these polarons are of sufficient size and number to overcome the percolation threshold, they can mediate long-range magnetic order in the system. This theory has been very successful in explaining the ferromagnetic behavior of many systems[6, 9, 10, 13] and opens avenues for developing new spintronic materials and gaining fundamental understanding about their behavior.

In this paper we report on a new DMD, based on samarium oxide (Sm_2O_3). Samarium oxide is a widely studied[14-18] high dielectric constant material and is known to exist in two different stable crystallographic phases, cubic or C-phase and monoclinic or B-phase. Our results showed that Cobalt doping in the B-phase polymorph of Sm_2O_3 results in a magnetic system that is free of secondary magnetic precipitates, but shows a similar magnetic response as that of a non- or weakly-interacting single domain (superparamagnetic) nanoparticle system. Quite interestingly we also found that the size of magnetic domains in this system varies with temperature, in contrast with conventional superparamagnetic materials.

Within the framework of polaron theory,[12] we propose a model to explain how a precipitate-free dilute magnetic dielectric can exhibit a supermagnet-like response with varying domain size. Our high resolution transmission electron microscopy (HRTEM) results revealed that in the Co doped Sm_2O_3 system the Co atoms are homogeneously distributed throughout the Sm_2O_3 matrix, but the polaron-inducing defects are inhomogeneously distributed, mostly aggregating at grain boundaries. These defect aggregates result in the formation of polaron clusters. Each "polaron cluster" acts as a single ferromagnetic domain possessing a supermoment.[19] These clusters are isolated from each other within a matrix where there is insufficient defect density for long-range magnetic interaction via polaron overlap, as illustrated in Fig. 3.1. This magnetism mimics that of nanoparticle super-paramagnets, but the origin of blocked single-domain response is completely different. Most importantly, the single domain defect cluster size is not determined by the particle or grain size of a nanoparticle system, rather it is a dynamic function of temperature.

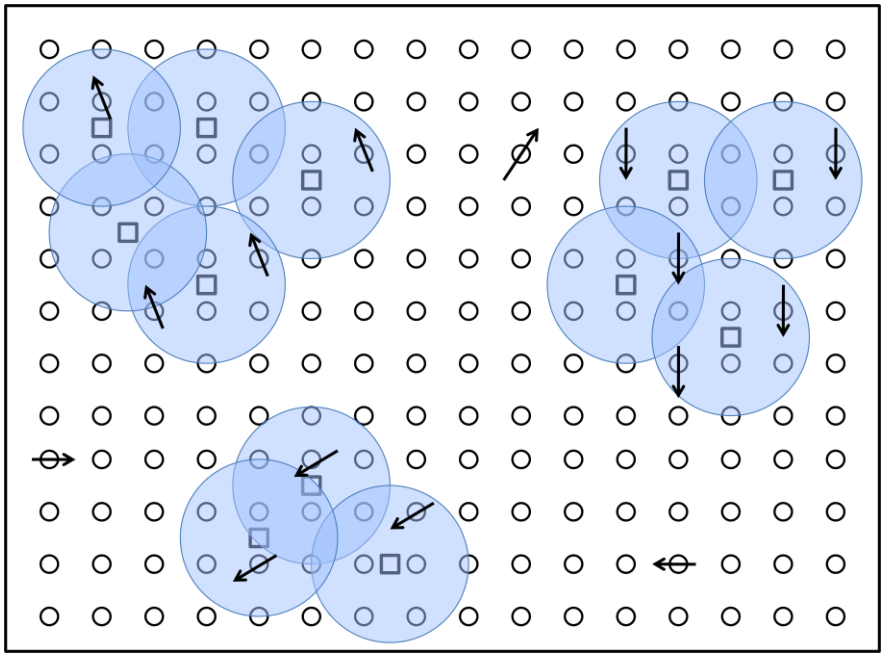

Figure 3.1: Schematic diagram illustrating defect clusters form isolated "superspins." Squares represent defects, arrows are magnetic dopant atoms, and transparent circles are the trapped electron orbital radius, or polaron radius.

3.3 Experimental Procedure

Thin films of $Sm_{2-x}Co_xO_3$ (x=0-0.1) were grown on $SrTiO_3$ (001) substrates using a pulsed laser deposition (PLD) technique. The $Sm_{2-x}Co_xO_3$ targets used for ablation were prepared by a sol-gel processing technique followed by isostatic pressing and sintering at 900 ^oC. A KrF excimer laser with 248 nm wavelength and 25 ns pulse-width was used. Substrate temperature was varied between 450 ^oC to 670 ^oC and depositions were made under low (10^{-6} torr) and high (10^{-1} torr) O_2 pressure environments. Care was taken at every step to avoid introducing magnetic contaminants into the system, including exclusive use of ceramic containers, ceramic spatula, and plastic tweezers. Films were characterized using high resolution X-ray diffraction (HRXRD), transmission electron microscopy (TEM), energy dispersive x-ray spectroscopy (EDS), and magnetic property measurements using Quantum Design Physical Property Measurement system (PPMS).

3.4 Results

In Fig. 3.2 we have shown the x-ray diffraction patterns of $Sm_{1.9}Co_{0.1}O_3$ films prepared at: **(a)** substrate temperature of 570 °C and O_2 pressure of 10^{-1} torr (hereafter referred as high oxygen pressure), **(b)** substrate temperature of 670 °C and O_2 pressure of 10^{-6} torr (hereafter referred as low oxygen pressure). From the diffraction pattern, the film prepared at high oxygen pressure was identified as C-phase with a cubic structure while the film prepared at low oxygen pressure was identified as B-phase with a monoclinic crystal structure. High oxygen pressure cubic $Sm_{1.9}Co_{0.1}O_3$ films showed very strong diffraction peaks corresponding to the (100) family of planes, indicating a

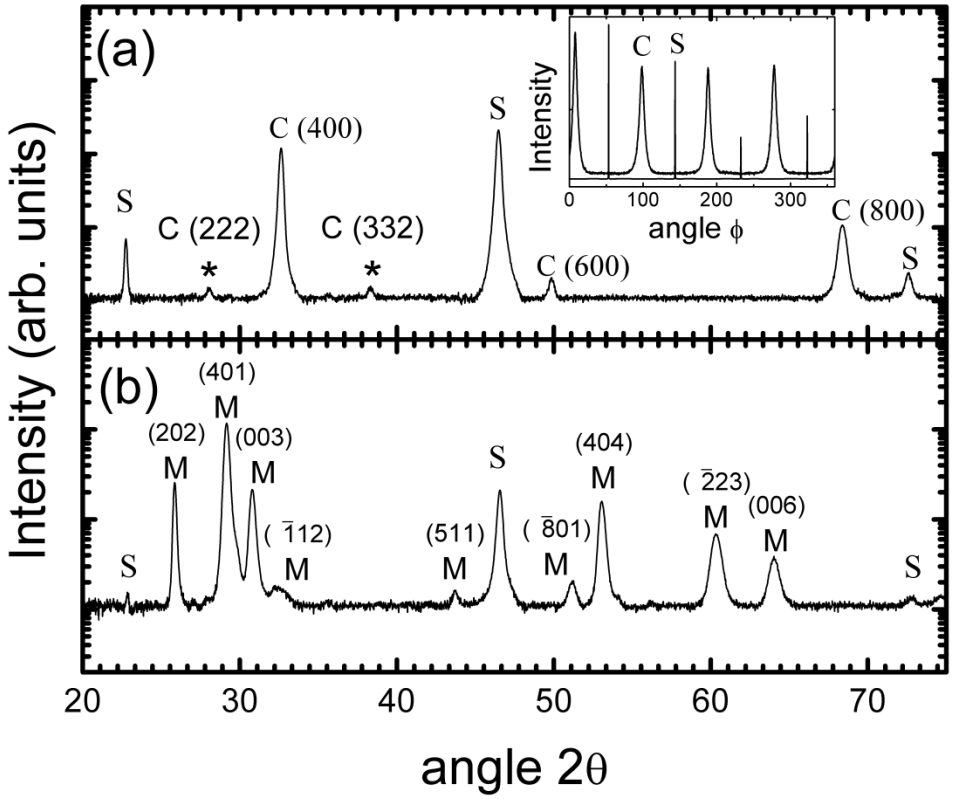

Figure 3.2: HRXRD θ-2θ scan for $Sm_{1.9}Co_{0.1}O_3$ thin films. (a) Scan for films deposited under 0.1 mbar O_2 pressure. 'S' peaks are from $SrTiO_3$ substrate, 'C' peaks are epitaxial cubic phase (C-phase) Sm_2O_3, and peaks labeled '*' are non-epitaxial C-phase Sm_2O_3. The inset shows Φ-scan on both $Sm_{1.9}Co_{0.1}O_3$ (404) and $SrTiO_3$ (101) reflections. (b) Scan for films deposited under 1×10-6 mbar O2 pressure. All 'M' labeled peaks belong to monoclinic (B-phase) Sm_2O_3.

strong a-axis alignment of the film. However, two additional weak peaks (possessing 3 orders of magnitude smaller intensity compared to strongest peak) belonging to other reflections of C-phase Sm_2O_3 were also observed, indicating the presence of some misoriented grains. Φ scan XRD of the (101) family of peaks (Fig. 3.2(a) inset) show a clear four-fold cubic symmetry, and 45° separation between substrate and film peaks. This indicates the growth of C-phase $Sm_{1.9}Co_{0.1}O_3$ film occurs with a 45° in plane rotation with respect to substrate.[18] The diffraction pattern of the monoclinic films showed them to be polycrystalline in nature. In both cases, cubic as well as monoclinic, all peaks resolved can be assigned to known Sm_2O_3 reflections indicating phase purity in the samples.

In order to further investigate the microstructure of the film and to search for signs of Co metal phase precipates (if any), Cross sectional TEM was performed. Low magnification bright field TEM, HRTEM, and selected area diffraction (SAD), were performed on both cubic and monoclinic $Sm_{1.9}Co_{0.1}O_3$ thin film samples. Bright field imaging was used to survey large regions of the films, especially near the interface where Co precipitates would be likely to form. These images showed a clean interface with no obvious signs of intermixing or secondary phases. HRTEM was used to further analyze regions from the film center, interface, and near the surface. Fig. 3.3(a) shows a typical HRTEM image of the interface of the cubic phase $Sm_{1.9}Co_{0.1}O_3$ film and STO substrate. Stacking faults are visible in this HRTEM image, however no Co grains were identified at the abrupt interface or within the film in any images taken. The SAD pattern in Fig. 3.3(b) was taken from film/substrate interface, with mostly film illuminated. The sample was rotated to show the film's [001] zone axis diffraction pattern. Indexing of the

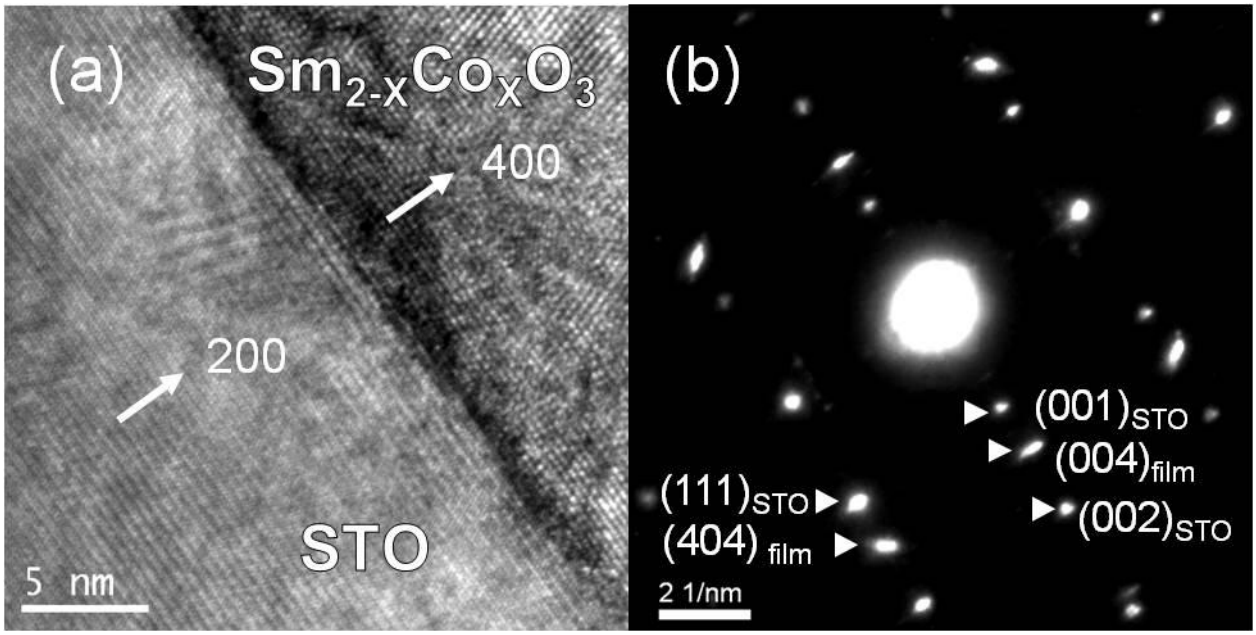

Figure 3.3: Results of TEM characterization. (a) Typical HRTEM image taken from interface of cubic phase $Sm_{1.9}Co_{0.1}O_3$ and $SrTiO_3$. (b) Selected Area Diffraction pattern of cubic phase film rotated to [100] zone axis, with substrate at [110] zone axis.

SAD pattern confirmed the 45° in-plane rotation in film growth established by XRD studies, with the following orientation relationships: $(004)_{Sm2o3}||(002)_{STO}$ and $[100]_{Sm2o3}||[110]_{STO}$. The SAD shows only peaks which are identified as Sm_2O_3 and $SrTiO_3$ reflections. We could not detect any additional diffraction spots that could be assigned to any Co phase.

The monoclinic phase $Sm_{1.9}Co_{0.1}O_3$ film was also extensively studied by HRTEM. Images at the interface appeared clean and crystalline, like those from the cubic film. Near the center of the monoclinic film the polycrystalline nature becomes apparent as multiple orientations and grain boundaries are visible. In Fig. 3.4(a) we have shown a typical HTREM image from the center region of the film, where a different crystal orientation occurs on each side of a grain boundary. Stacking faults are also present, which propagate from the grain boundary into the crystal structure of the grain. From all the images taken we infer that monoclinic film has a much higher defect density in the form of grain boundaries and other faults around the grain boundaries when compared with the cubic phase film (where no misoriented grains or boundaries could be found). This can be attributed to the inability of monoclinic phase to form a closely matched lattice with the substrate, as well as oxygen vacancies due to the oxygen deficient environment required during deposition. Indexing the SAD pattern for this film again found only peaks identified as Sm_2O_3 and $SrTiO_3$ reflections as shown in fig. 3.4(b). Multiples of one diffraction spot with different angular orientation about the zeroth order spot are found, confirming the presence of multiple Sm_2O_3 grains with varied orientation.[20]

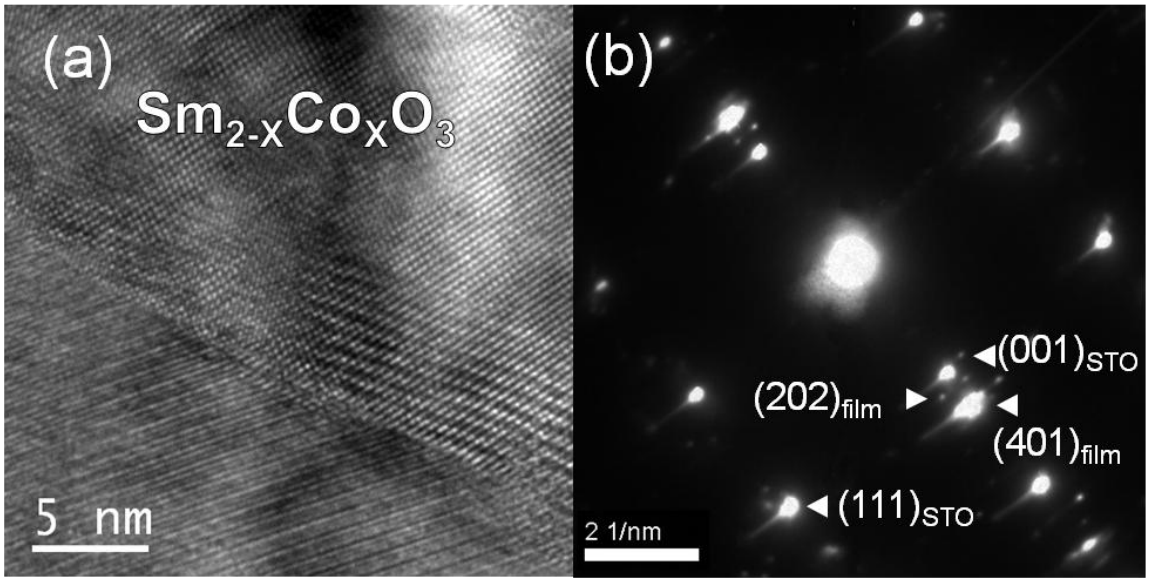

Figure 3.4: Results of TEM characterization. (a) Typical HRTEM image taken from monoclinic phase $Sm_{1.9}Co_{0.1}O_3$ film. (b) Selected Area Diffraction pattern of monoclinic phase film with substrate at [110] zone axis.

Magnetization (M) *vs*. applied field (H) measurements on $Sm_{1.9}Co_{0.1}O_3$ films showed some very interesting characteristics. In Fig. 3.5 we have shown the M *vs*. H data for (a) cubic and (b) monoclinic phase films at temperatures varied from 10K to 200K. Insets show the M *vs*. H curves for undoped Sm_2O_3 films at 10K for both (a) monoclinic and (b) cubic phases. The undoped films were deposited and measured under identical conditions as doped films, and show only a weak paramagnetic response resulting from unpaired f-electrons in Sm cations.[21] Because the thin films were deposited on diamagnetic substrates with mass many orders of magnitude higher, the (linear) magnetic contribution must be taken into account. The data reported for thin films of Sm_2O_3 have had the calculated diamagnetic contribution subtracted out so that only the magnetism of the film is considered. The data reported for $Sm_{1.9}Co_{0.1}O_3$ thin films have the linear component consisting of both the diamagnetic substrate and paramagnetic background terms subtracted from the data reported, so that the langevin function can be used to fit only the magnetism of the doped film.

The M *vs.* H data of the monoclinic $Sm_{1.9}Co_{0.1}O_3$ films show a clearly visible hysteretic behavior below 200K. A coercivity value as high as ~3000 Oe was observed at 10K. This extremely large coercivity drops quickly as temperature increases and vanishes at 200K, though the M *vs.* H data still exhibit a saturation effect. Cubic phase $Sm_{1.9}Co_{0.1}O_3$ films also show magnetic saturation. However, the saturated magnetic moment is much smaller than that of monoclinic $Sm_{1.9}Co_{0.1}O_3$ films, and cubic films exhibit almost no detectable coercivity.

In order to further investigate the magnetic behavior of $Sm_{1.9}Co_{0.1}O_3$ films we performed the field cooled (FC) and zero field cooled (ZFC) Magnetization *vs.*

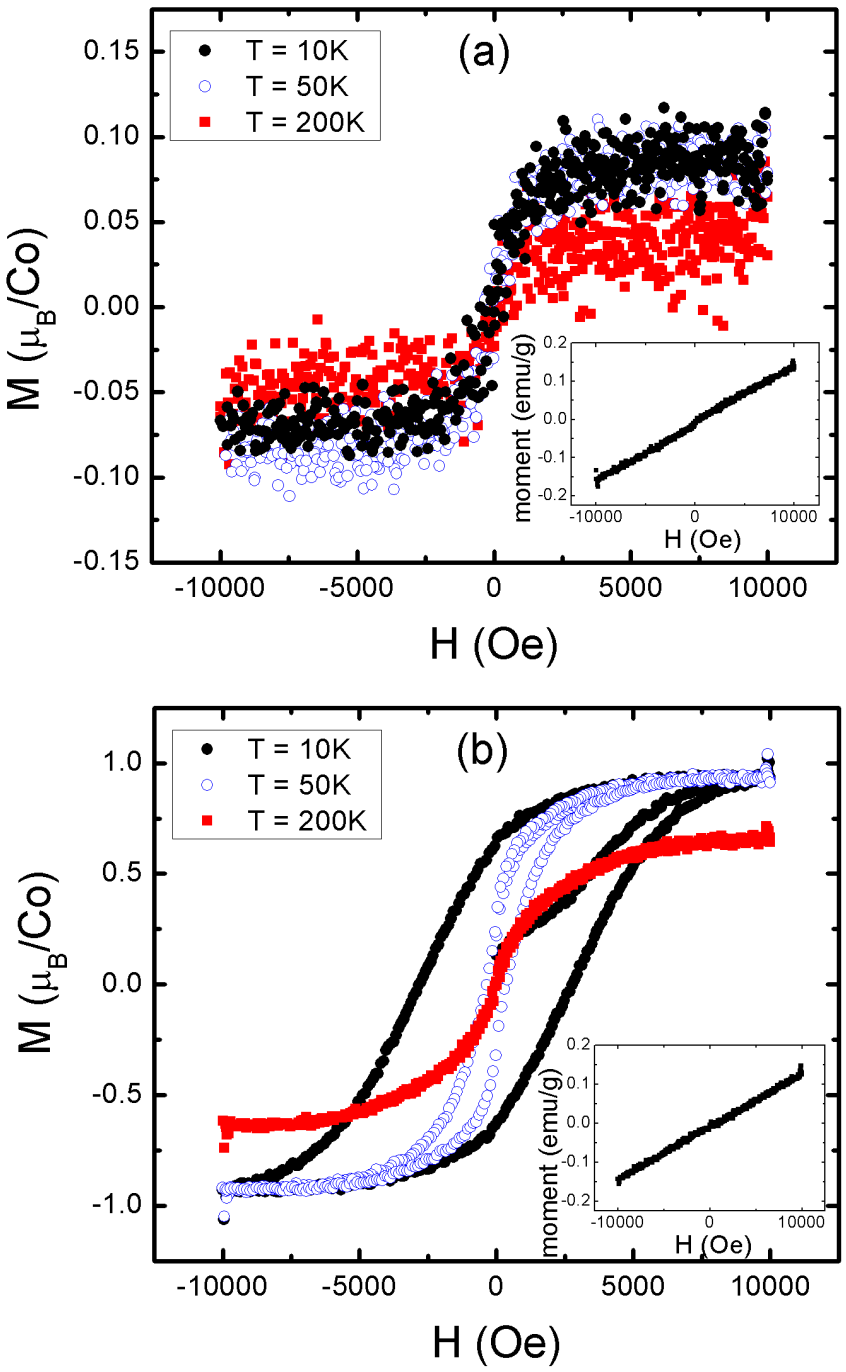

Figure 3.5: Magnetization M *vs.* applied field H for (a) cubic phase and (b) monoclinic phase $Sm_{1.9}Co_{0.1}O_3$ thin films. Insets show M *vs*. H for undoped Sm_2O_3 films for each respective phase.

Temperature (M *vs*. T) measurements (see Fig. 3.6). The ZFC/FC M *vs*. T data exhibit three salient features: (1) ZFC and FC data show bifurcation at about 130 K, indicating single domain magnetic particles.[22] (2) The bifurcation occurs at a temperature above the peak in the ZFC data, indicating that there is a gradual onset of superparamagnetic blocking, and hence a large distribution of different particle shapes and sizes.[23] (3) The FC data show a minimum at about T=40K, whereas the FC measurement of a conventional superparamagnet should never decrease with decreasing temperature.[24, 25] This slight decrease and minimum is likely due to weak interactions between superspin clusters, as well as isolated paramagnetic spins throughout the sample.[25, 26]

3.5 Discussion

3.5.1 Origin of Magnetic Response

The M *vs*. H data for $Sm_{1.9}Co_{0.1}O_3$ films show characteristics of single domain magnetic nanoparticles system. However, M *vs*. T and structural characterization data showed that the present material is not a clear cut example of a superparamagnetic system and much more complex physical mechanisms are at work. In general, the origin of supermagnetism is usually ascribed to precipitates of magnetic metal formed in a matrix due to low solubility. For this magnetic precipitate scenario the grain size of a superparamagnetic particle can be calculated using the experimentally determined blocking temperature T_B in the relation $KV=25k_BT_B$,[3, 27] where K is the bulk anisotropy energy, V is volume of particle, k_B is Boltzmann's constant. If we assume that in $Sm_{1.9}Co_{0.1}O_3$ films the magnetic dopant (Co in this case) is precipitating out of solution and calculate the approximate diameters of the precipitates, numbers come as 70 Å for

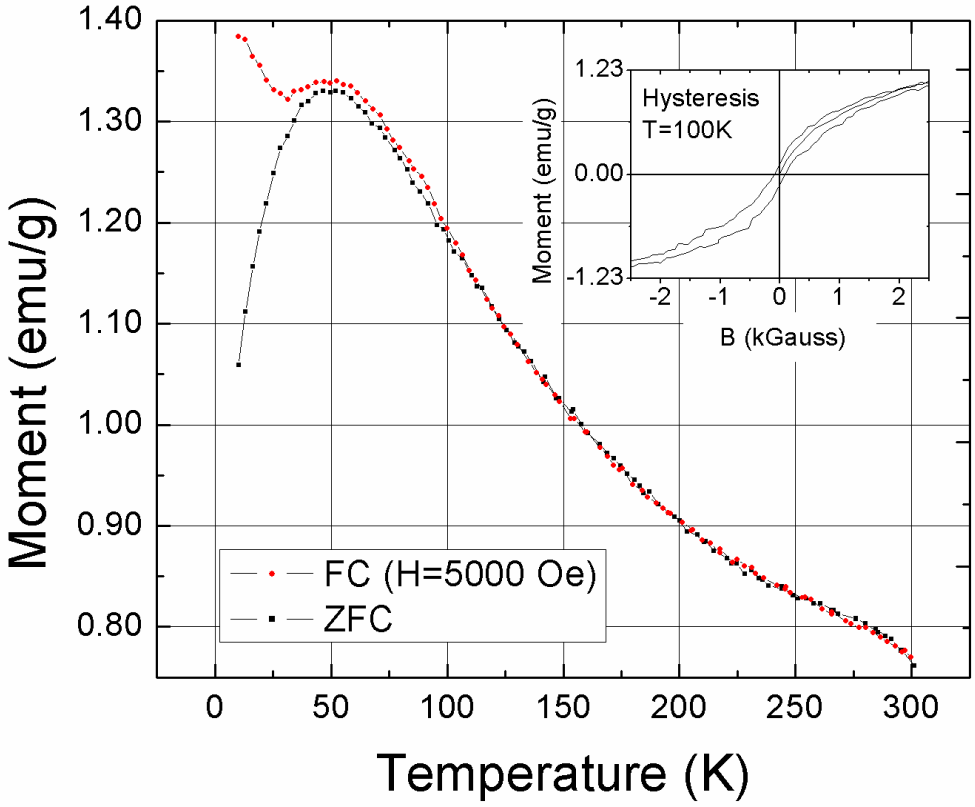

Figure 3.6: Zero field cooled (ZFC) and field cooled (FC) measurements of magnetic moment *vs*. temperature, for monoclinic phase $Sm_{1.9}Co_{0.1}O_3$ thin films grown under vacuum. Inset shows M *vs.* applied field H for monoclinic phase $Sm_{1.9}Co_{0.1}O_3$ thin film at 100 K, with hysteresis indicating that T_B is above T=100K.

monoclinic film and 25 Å for the cubic film. In the above calculation we have assumed the anisotropy energy (K) of Co as $4x10^6$ erg/cm^3, and the values of T_B for monoclinic and cubic films as 200K and 10K, respectively, based on the temperature at which hysteresis in M *vs.* H disappears.

Cobalt granules 70 Angstroms and even 25 Angstroms in diameter as calculated from the anisotropy relation should be easily resolvable in our high resolution TEM if present. Further, the density difference between Co metal (8.79 g/cm^3) and Sm_2O_3 (7.74 g/cm^3 and 7.07 g/cm^3 for monoclinic and cubic, respectively) should also give a clear contrast difference, meaning Co should be detectable in bright field and high resolution TEM without difficulty. A careful and comprehensive investigation of both phases of $Sm_{1.9}Co_{0.1}O_3$ films under HRTEM and bright field TEM yielded no such evidence.

Although no Co precipitates that could account for the magnetism were observed in XRD and TEM, this does not completely rule out the possibility of compositional variation of Co throughout the Sm_2O_3. The film could form coherent Co-rich nanocrystals (at a surface or other feature,) within a Co-poor crystal matrix.[28] Since the structure and orientation of these crystals are the same, and density varies only slightly, they can be invisible to conventional analysis techniques. A good example of the formation of coherent dopant rich antiferromagnetic nanocrystals with unquenched spins at the film surface is discussed in detail for $Zn_xCo_{1-x}O$ by Dietl *et al*.[29] However, we believe that if the same is happening in $Sm_{1.9}Co_{0.1}O_3$, there should be a stronger correlation between the magnetic response of both cubic and monoclinic samples, since both have the same ratio of Co dopant. Furthermore, as will be shown in the following

sections, the temperature dependence of the magnetization data cannot be explained by just assuming the presence of static clusters with temperature independent size.

3.5.2 Implications from Temperature Dependent M *vs.* H and Coercivity Data

In order to further investigate the actual mechanism responsible for magnetism in the material, the M *vs*. H data at temperatures above T_B were fitted to the Langevin function[30]

$$M = Nm\left[\coth\left(\frac{mH}{k_BT}\right) - \frac{k_BT}{mH}\right] \quad (3.1)$$

where M is the total magnetization, N is the number of magnetic spins (paramagnet) or superspins (superparamagnet), m is the moment per spin or superspin. H is the applied field, T is temperature, and k_B is Boltzmann's constant.

Figure 3.7 shows the experimental M *vs*. H data fitted to the Langevin function and Table 3.1 enumerates the fitting parameters. As can clearly be seen in Fig. 3.7, the data fits quite well to Langevin's function. The third column in Table 3.1 shows the value of the magnetic moment of single clusters while the fourth column gives an estimate of the number of Co atoms participating in each single domain cluster. Here we have assumed that each cobalt is in the high spin state and contributes a moment of 4.8 μ_B. As can be seen in Table 3.1, $Sm_{1.9}Co_{0.1}O_3$ films exhibit a drastic decrease in the magnetic moment per cluster as temperature decreases. The decrease in *m* indicates that fewer Cobalt ions are incorporated into each cluster at lower temperatures, implying that the size of magnetically active cluster decreases with decrease in temperature.

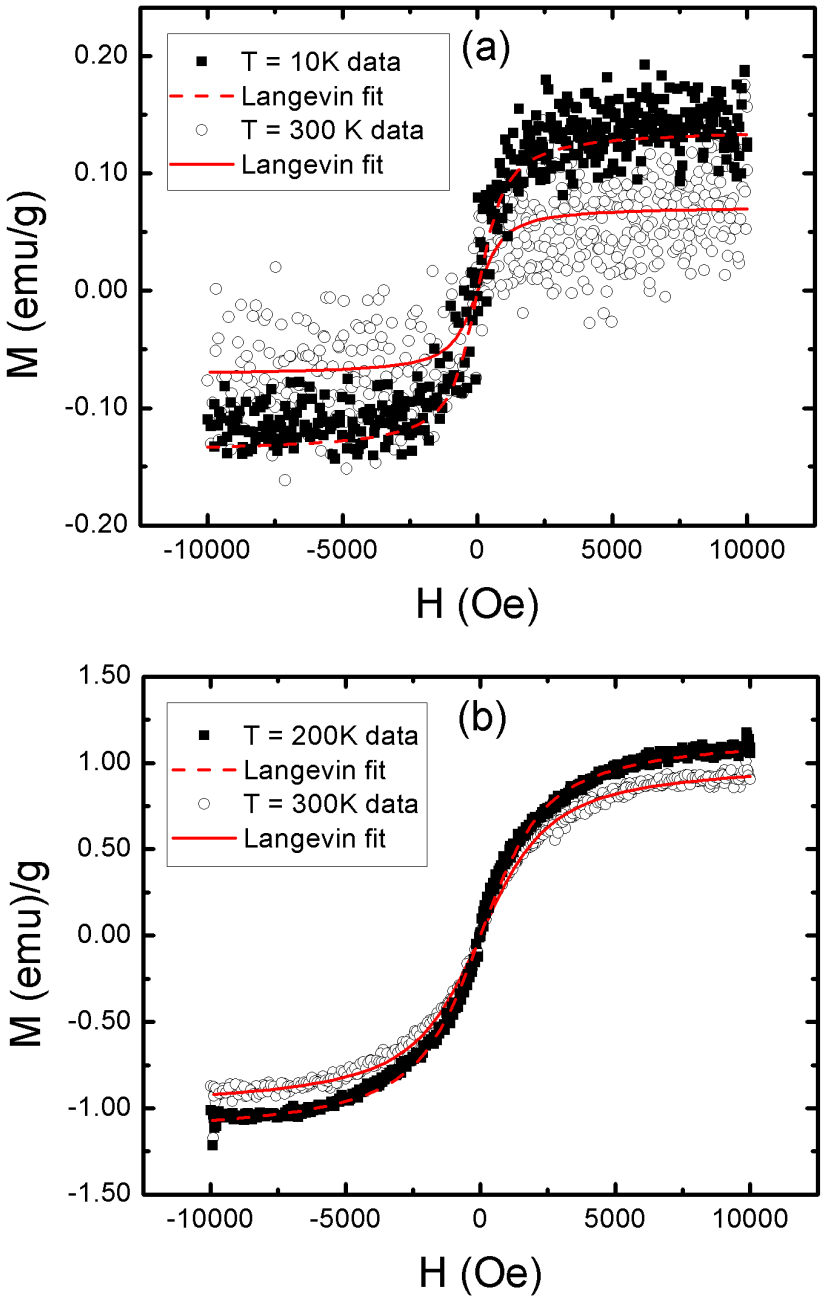

Figure 3.7: Langevin function fit to experimental data for: (a) cubic and (b) monoclinic $Sm_{1.9}Co_{0.1}O_3$ films.

Table 3.1: Fitting parameters from experimental M *vs*. H data fitted to the Langevin function. N is the number of magnetic superspins, *m* is the moment per superspin, and the fourth column gives and estimation of the number of Co ions incorporated per superspin cluster.

Monoclinic Film					
Temp. (K)	N (clusters/g)		*m* (μ_B/cluster)		Co^{2+} ions/cluster
300	2.45×10^{16}	$\pm0.04\times10^{16}$	4508	±55	940
200	3.95×10^{16}	$\pm0.05\times10^{16}$	3225	±36	672
Cubic Film					
300	6.55×10^{14}	$\pm1.56\times10^{14}$	11,900	±2,500	2517
200	7.62×10^{14}	$\pm1.50\times10^{14}$	10,380	±1,870	2163
100	1.73×10^{15}	$\pm0.24\times10^{15}$	5830	±760	1122
10	3.91×10^{16}	$\pm0.33\times10^{16}$	382	±29	80

In the case of a canonical superparamagnetic system, the magnetic coercivity data below the blocking temperature follow the relation: [31]

$$H_C = H_{C0}\left[1 - \left(\frac{T}{T_B}\right)^{1/2}\right] \tag{3.2}$$

where T_B is the blocking temperature, T is the temperature, and H_{C0} is the coercivity at T=0 K. In Fig. 3.8, we have shown the coercivity data for the monoclinic film and the fit to Eq. (3.2) (blue dashed line). As can clearly be seen, experimental data do not show any agreement with Eq. (3.2), indicating that this material cannot be treated as a canonical superparamagnet. As will be shown in next section, the temperature dependence of corecivity can be accounted for if we assume that the size of magnetic clusters changes with temperature following the defect mediated exchange mechanism proposed by Coey *et al.* [12]

According to the Coey *et al.* theory, electrons in dilute magnetically doped insulating systems can become bound by defects to form hydrogen-like "polarons."[12] When these polarons are of sufficient size and number to overcome the percolation threshold, they can mediate long-range magnetic order in the system. We expect that even in the cases when polarons are not of sufficient number to result in complete long range ferromagnetic ordering, they can still result in the formation of localized magnetically active cluster. In order to determine the temperature dependence of magnetic coercivity in this situation we substituted the expression for blocking temperature, $T_B = KV/25k_B$,[27] into Eq. (3.2). We assume a particle composed of n spherical polarons, so $V = n\frac{4}{3}\pi r^3$. N is the effective number of polarons composing each particle, and 'r' is the hydrogenic orbital radius of a polaron. The radius 'r' is a

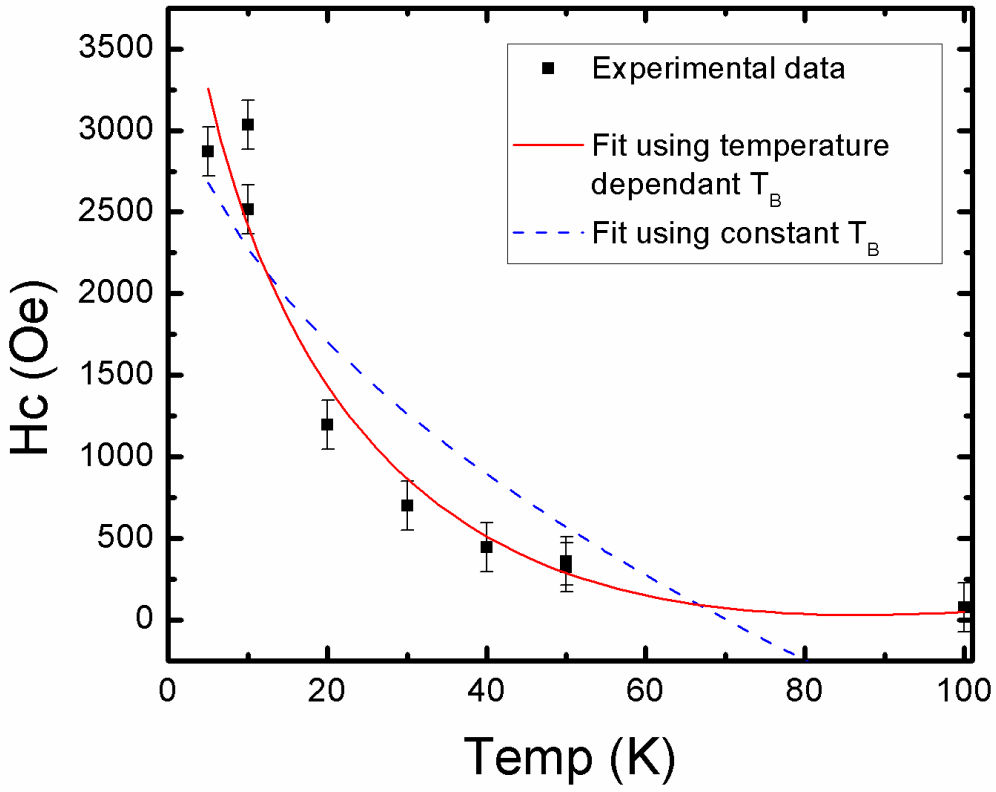

Figure 3.8: Coercive field strength *vs*. temperature for monoclinic $Sm_{1.9}Co_{0.1}O_3$. The data fits using the unmodified and modified coercivity equation for superparamagnets are also shown (Eq. (3.2) and Eq. (3.3) respectively).

function of dielectric constant 'ε' following the relation $r=\varepsilon(m/m^*)a_0$,[12] where m is the electron mass, m^* is the effective mass of the donor electrons and a_0 is the Bohr radius (53 pm). Assuming that the effective electron mass is same as the free electron mass, the polaron radius can be approximated as $r = a_0\varepsilon$. Since the dielectric constant 'ε' is a function of temperature, the polaron exchange mechanism can result in magnetic clusters that change their size as the temperature changes. Assuming a simple first order temperature dependence of dielectric constant $\varepsilon(T) = \varepsilon_{T0} + \alpha T$, Eq. (3.2) reduces to:

$$H_C = H_{C0}\left[1 - \left(\frac{25k_BT}{nK\frac{4}{3}\pi {a_0}^3(\varepsilon_{T0}+\alpha T)^3}\right)^{\frac{1}{2}}\right] \tag{3.3}$$

Equation 3 fitted to the coercivity data is shown by the solid red line in Fig. 3.8. A good quality of fit can clearly be visualized. In the above fit we used the experimentally determined value of 'α' [32] while 'H_{C0}', 'ε_{T0}' and 'nK' (anisotropy energy per particle times the number of polarons in each cluster) were kept as the free parameters. For the best fitting the values of the fitting parameters 'H_{C0}', 'ε_{T0}' and 'NK' were found to be 5616.7 gauss, 2.63, 7.83×10^9 erg/cm^3, respectively. Using the value of 'ε_{T0}'and α, the value of room temperature dielectric constant of the material was estimated to be 7.25, which matches very well with the value of 7.3 reported in literature for polycrystalline monoclinic Sm_2O_3. [14]

All of the above analysis supports our hypothesis that the size of magnetically active clusters changes with temperature. Specifically, we have observed that the increase of cluster size is a direct consequence of the increase in the polaron radius. This is consistent with the experimental finding that increasing numbers of Co ions are incorporated into the clusters as the temperature (and hence the volume of the cluster)

increases. The total number of clusters (N) decreases as groups of smaller clusters merge to form larger cluster once their volumes overlap. Though Co dopant levels are the same, the enhanced magnetic response of polycrystalline monoclinic film compared with cubic film indicates that a greater number of polaron inducing defects are present, supporting the same conclusion made from analysis of the TEM results.

3.6 Summary

To summarize, we have grown Co doped Sm_2O_3 thin films by the pulsed laser deposition technique. The films grown at lower oxygen pressure were found to have polycrystalline monoclinic structure, while the films grown at higher oxygen pressure showed cubic structure. Monoclinic films had a much higher defect density than the cubic films, and exhibited a stronger magnetic response. Further, we found that $Sm_{1.9}Co_{0.1}O_3$ films exhibit very intriguing magnetic behavior which cannot be explained using the conventional superparamagnetic theory. Specifically, $Sm_{1.9}Co_{0.1}O_3$ films show magnetic properties similar to single domain weakly interacting clusters, even though no secondary phases or compositional variation were detected. Magnetic behavior of the films was explained by assuming the presence of magnetically active nonpercolating regions resulting from the polaron mediated exchange mechanism. Since the interaction responsible for polaron cluster formation is temperature dependant, the size of the clusters changes with temperature, as reflected in the M *vs*. H and H_C *vs*. T data.

3.7 References

1. G. A. Prinz, Science **282**, 1660 (1998).

2. S. A. Wolf, D. D. Awschalom, R. A. Buhrman, J. M. Daughton, S. von Molnar, M. L. Roukes, A. Y. Chtchelkanova, and D. M. Treger, Science **294**, 1488 (2001).

3. W. K. Park, R. J. Ortega-Hertogs, J. S. Moodera, A. Punnoose, and M. S. Seehra, J. Appl. Phys. **91**, 8093 (2002).

4. J. M. D. Coey, M. Venkatesan, P. Stamenov, C. B. Fitzgerald, and L. S. Dorneles, Phys. Rev. B: **72**, 024450 (2005).

5. J. Ran and Z. Yan, J. Semicond. **30**, 102002 (2009).

6. S. J. Pearton, et al., J. Phys.: Condens. Matter **16**, R209 (2004).

7. T. Sasaki, S. Sonoda, Y. Yamamoto, K.-i. Suga, S. Shimizu, K. Kindo, and H. Hori, J. Appl. Phys. **91**, 7911 (2002).

8. H. Kimura, T. Fukumura, M. Kawasaki, K. Inaba, T. Hasegawa, and H. Koinuma, Appl. Phys. Lett. **80**, 94 (2002).

9. A. Tiwari, V. M. Bhosle, S. Ramachandran, N. Sudhakar, J. Narayan, S. Budak, and A. Gupta, Appl. Phys. Lett. **88**, 142511 (2006).

10. B. Vodungbo, Y. Zheng, F. Vidal, D. Demaille, V. H. Etgens, and D. H. Mosca, Appl. Phys. Lett. **90**, 062510 (2007).

11. A. L. Efros and M. Pollack, *Electron-electron Interactions in Disordered Systems* (Elsevier Science Pub., 1985).

12. J. M. D. Coey, M. Venkatesan, and C. B. Fitzgerald, Nature Mater. **4**, 173 (2005).

13. Y. Zheng, B. Vodungbo, F. Vidal, M. Selmane, and D. Demaille, J. Cryst. Growth **310**, 3380 (2008).

14. A. A. Dakhel, J. Alloys Comp. **365**, 233 (2004).

15. J. Paivasaari, M. Putkonen, and L. Niinisto, Thin Solid Films **472**, 275 (2005).

16. V. A. Rozhkov, A. Y. Trusova, and I. G. Berezhnoy, Thin Solid Films **325**, 151 (1998).

17. K. Shalini and S. A. Shivashankar, Bull. Mater. Sci. **28**, 49 (2005).

18. H. Yang, H. Wang, H. M. Luo, D. M. Feldmann, P. C. Dowden, R. F. DePaula, and Q. X. Jia, Appl. Phys. Lett. **92** (2008).

19. S. Bedanta and W. Kleemann, J. Phys. D: **42**, 013001 (2009).

20. B. Fultz and J. M. Howe, *Transmission Electron Microscopy and Diffractometry of Materials* (Springer Berlin Heidelberg New York, 2008).

21. C. Kittel, *Introduction to Solid State Physics* (John Wiley & Sons, Inc., 1995).

22. M. F. Hansen and S. Mørup, J. Magn. Magn. Mater. **203**, 214 (1999).

23. T. Bitoh, K. Ohba, M. Takamatsu, S. Takashi, and S. Chikazawa, J. Phys. Soc. Jpn. **64**, 1305 (1995).

24. M. Sasaki, P. E. Jonsson, H. Takayama, and H. Mamiya, Phys. Rev. B: **71** (2005).

25. O. Petracic, X. Chen, S. Bedanta, W. Kleemann, S. Sahoo, S. Cardoso, and P. P. Freitas, J. Magn. Magn. Mater. **300**, 192 (2006).

26. X. Chen, S. Bedanta, O. Petracic, W. Kleemann, S. Sahoo, S. Cardoso, and P. P. Freitas, Phys. Rev. B: **72** (2005).

27. C. P. Bean and J. D. Livingston, J. Appl. Phys. **30**, 120S (1959).

28. T. Dietl, Physica E **35**, 293 (2006).

29. T. Dietl, T. Andrearczyk, A. Lipinska, M. Kiecana, M. Tay, and Y. Wu, Phys. Rev. B: **76**, 155312 (2007).

30. N. Spaldin, *Magnetic Materials: Fundamentals and Device Applications* (Cambridge University Press, 2003).

31. B. D. Cullity and C. D. Graham, *Introduction to Magnetic Materials* (Hoboken, N.J.: IEEE/Wiley, 2009).

32. The value of 'α' was determined experimentally for Sm2O3:Co by doing temperature dependent capacitance (C) measurements on a sintered pellet near room temperature. By fitting the capacitance data to the linear ratio C= C0 + αT the value of 'α' was estimated to be 0.015.

CHAPTER 4

STRUCTURAL AND DIELECTRIC PROPERTIES OF EPITAXIAL Tb_2O_3 INSULATING FILMS

4.1 Abstract

We have grown high quality Tb_2O_3 thin films with on a variety of substrates, and shown enhanced dielectric constant related to improved crystal quality compared with previous reports. Growth in an oxygen rich environment yields nearly single crystal C-phase thin films, which can be grown either in (001) or (111) orientation depending on the substrate lattice parameter. Using low oxygen pressure a different morphology, B-phase Tb_2O_3 can be achieved. The dielectric constant of these films depends on the morphology, and the cubic phase epitaxial film shows an enhanced dielectric constant of $k = 25$.

4.2 Introduction

High-k replacements for SiO_2 as gate dielectrics in complementary metal oxide semiconductor (CMOS) devices have recently been widely studied, with no single candidate emerging problem free. Due to thermodynamic instability with Si, all high-k

TM oxides except Hf and Zr have been ruled out, but these have low recrystallization temperatures which limit the thermal budget and post-annealing processes of CMOS fabrication.[1, 2] Rare Earth oxides (REO) are considered promising candidates for this application due to their high resistivity, dielectric constants, large band gaps, and thermodynamic stability with silicon.[3, 4] La_2O_3, Sm_2O_3, and CeO_2 have been widely investigated, with dielectric constants reported ranging from 8-52.[5-8] The dielectric constant of thin films is usually significantly increased compared with bulk. Recently, Yang reported single crystal Sm_2O_3 films with a dielectric constant of 30.5,[9] and discussed the effect of crystallinity on increasing the dielectric constant from the bulk value 7.3.[8]

We report the growth of another REO system, Tb_2O_3, which also shows a greatly improved dielectric constant with high quality epitaxy. The dielectric constant for bulk Tb_2O_3 has been reported as k = 13.43 for cubic in theory[10] and k =13.3 experiment.[11] Previous reports for thin film Tb_2O_3 give values ranging from k = 6-10 for polycrystalline cubic (C) phase films grown on Silicon by pyrolysis.[12] Our growth method can produce both polycrystalline and highly oriented Tb_2O_3 thin films on several substrates including Si, and confirm that the epitaxial film shows a marked improvement in the dielectric constant, from k = 13.0 for polycrystalline monoclinic films to k = 24.5 for cubic oriented films, at low frequencies.

4.3 Experimental Procedure

Tb_2O_3 thin films were produced by pulsed laser deposition (PLD). A target was made by pressing mixed valence Tb_4O_7 powder (available from Alfa Aesar) and sintering

at 1400° C for 12 hours. Thin films were then deposited by ablating the densified powder target pellet with a 248 nm KrF excimer laser with 25 ns pulsewidth. Substrate temperature was varied from 500° C to 600° C and depositions were made under (a) low O_2 pressure (10^{-6} torr) and (b) high O_2 pressure (10^{-1} torr). In order to test growth on a variety of substrates, films were deposited on MgO, $LaAlO_3$, $SrTiO_3$, and Si(100) single crystals purchased from MTI.

Film structures were characterized using x-ray diffraction (XRD) and cross sectional Transmission Electron Microscopy (TEM). The optical transmission was measured using a Shimadzu model 1240 UV-vis spectrophotometer, from which the bandgaps were calculated. The dielectric properties measurements were performed on Tb_2O_3 thin films grown on conductive Nb:$SrTiO_3$ single crystal substrates by PLD. An approximately 100x100 micron probe tip was the top contact, and frequency dependent capacitance measurements were made using a HP 4284A precision LCR meter, from which the dielectric constant was calculated.

4.4 Results and Discussion

The θ-2θ scan x-ray diffraction patterns (XRD) of Terbium oxide films grown under high (10^{-1} torr) O_2 pressure oxygen atmosphere at 500° C are shown in Fig. 4.1(a). From the diffraction pattern all of these films were identified as cubic phase (C-type) Tb_2O_3. We saw only the (111) family of Tb_2O_3 peaks with the (001) family of substrate peaks for films grown on MgO and Si. For the films grown on $LaAlO_3$ and $SrTiO_3$ we saw only (001) family of peaks from both substrate and Tb_2O_3, indicating that the film and substrate have the same c axis orientation. In both cases the film quality was very

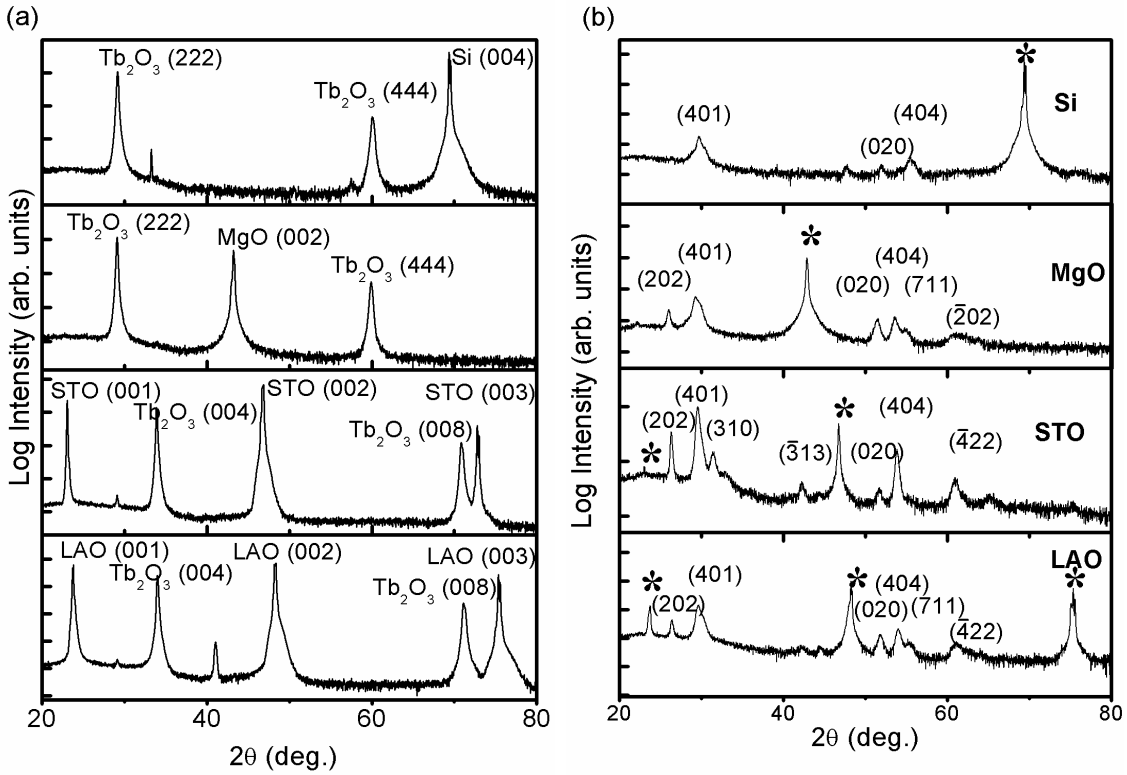

Figure 4.1: XRD θ-2θ scan for (a) films grown on Si, MgO, $SrTiO_3$ and $LaAlO_3$ substrates under 0.1 Torr oxygen pressure, and (b) films grown on the same substrates under $1x10^{-6}$ Torr oxygen pressure.

high, with film peak intensity approximately six orders of magnitude greater than the baseline. Fig. 4.1(b) shows XRD scans of the Tb_2O_3 films grown under low (10^{-6} torr) O_2 pressure with 600 °C substrate temperature on Mgo, Si, $SrTiO_3$, and $LaAlO_3$. XRD patterns taken from all of these films show peaks indicating polycrystalline monoclinic phase (B-type) of Tb_2O_3 with several orientations along the substrate c-axis. We conclude that oxygen pressure plays an import role determining the Tb_2O_3 film phase formed during growth, and in the cubic films the orientation is determined by the substrate lattice.

To determine the optical properties and the band gap UV-Vis spectroscopy was performed. MgO substrate was used to study optical properties as it has a very wide band gap, and showed highly oriented epitaxial growth as well. The polycrystalline monoclinic phase film shows high optical transmission for wavelengths above 390 nm, as shown in Fig. 4.2. The band gap was calculated by fitting absorption to the relation:

$$\alpha = C(h\nu - Eg)^n$$

where α is absorption, n=1/2 for direct band gaps, Eg is the energy band gap, ν is the frequency, h is Planck's constant, and C is a constant. From the absorption spectra the bang gap of B-phase monoclinic Tb_2O_3 was calculated to be 3.91 eV. This is value is consistent with other literature where polycrystalline Tb_2O_3 is measured.[13] This energy gap is understood to originate from the transition from the localized filled f-level in Tb sitting above the valence band (O 2p) to the unoccupied Tb 5d conduction band.[14, 15]

The cubic phase Tb_2O_3 thin film grown under oxygen pressure shows a reduced bandgap, calculated by the above method to be 2.66 eV. The origin of this decreased bandgap has not previously been reported, likely due to the lack of highly oriented single

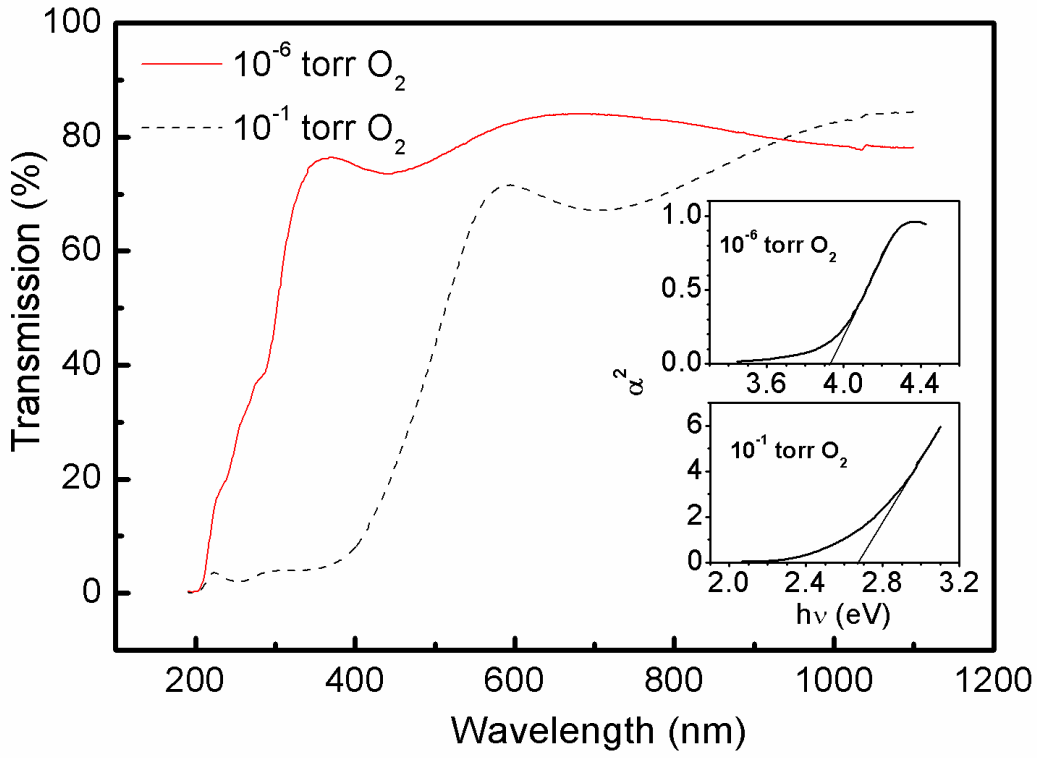

Figure 4.2: Optical transmission spectrum of Tb_2O_3 thin films grown on MgO substrate under O_2 and vacuum. Insets show bandgap calculation by plotting absorption α^2 vs $h\nu$.

crystalline thin films. The origin of this reduction is likely due to crystalline anisotropy, resulting in a different absorption mechanism along a single orientation than is observed in polycrystalline or bulk material. This could also be attributed to midgap defect states introduced to relieve strain during growth in the single crystal lattice.

Cross sectional TEM, including low magnification bright field TEM and high resolution TEM (HRTEM), and selected area diffraction (SAD), was performed on Tb_2O_3 thin film samples grown under high oxygen pressure in order to study the crystal growth and quality in detail. The bright field images of both films show a clean interface with no obvious signs of intermixing. Thickness measured by bright field imaging was 260 nm for both films grown on STO and MgO.

Fig. 4.3(a) shows the SAD pattern of C-phase Tb_2O_3 film grown on $SrTiO_3$ substrate. From the diffraction pattern the out of plane orientation relationship $(002)_{substrate}||(004)_{Tb2O3}$ is confirmed. The zone axis of the film is identified as [001], and substrate zone axis [110], giving the in plane orientation $(110)_{substrate}||(100)_{Tb2O3}$. This indicates that the film grown on $SrTiO_3$ have a 45° in-plane rotation with respect to the substrate.[16] In this direction, two substrate lattice spaces approximately match to one film lattice space. By this growth mechanism the calculated misfit is less than 3% for $SrTiO_3$. Films grown on $LaAlO_3$ have the same orientation and therefore should share the same growth mechanism, having a calculated lattice mismatch of about -.01%.

Fig. 4.3(b) shows high resolution TEM of the film/substrate interface. The film appears to form a coherent interface with the substrate, with no obvious grain boundaries or impurities, indicating good crystallinity.

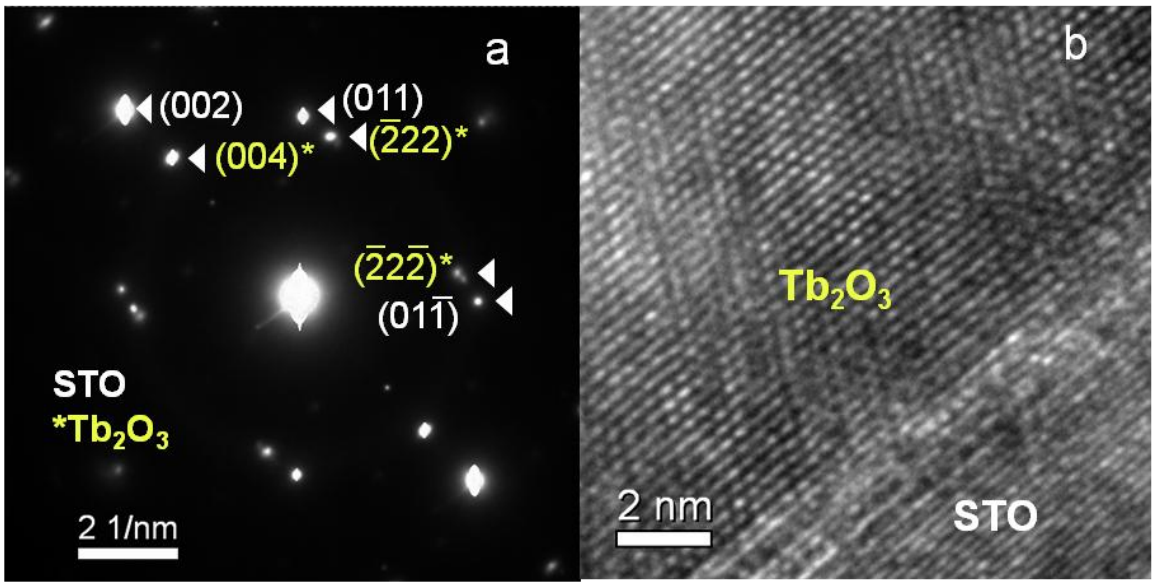

Figure 4.3: Results of TEM characterization. (a) SAD pattern of Tb_2O_3 film on $SrTiO_3$ substrate showing film [100] zone axis and substrate [110] zone axis. (b) HRTEM of interface between Tb_2O_3 film on $SrTiO_3$ substrate.

Fig. 4.4(a) shows SAD for Tb_2O_3 grown on MgO substrate. Out of plane orientation of this film is characterized by $(002)_{substrate}||(222)_{Tb2O3}$. The indexed zone axes are [100] for the substrate and [321] for the film, giving in-plane orientation to be $(100)_{substrate}||(321)_{Tb2O3}$. SAD patterns from both films confirm very high quality oriented crystal is grown, with little to no misorientation. HRTEM shown in Fig. 4.4(b) again shows an abrupt interface and good orientation between the film and substrate. Some contrast changes in this image may be due to line defects, but are likely due to damage from local heating introduced during sample preparation by milling with focused ion beam, which was seen throughout this film and substrate. Since the x-ray diffraction pattern of films grown on MgO was identical to those grown on Si substrates, the orientation relationships of both films are assumed to be the same.

The dielectric constant is dependent on crystal structure, thickness, and degree of crystallinity.[4] In polycrystalline films, grain size and orientations vary greatly yielding irreproducible results. Grain boundaries can serve as conduction pathways, leading to capacitance leakage.[17] Several studies have also shown that nearly-single oxide crystal films grown epitaxially have much higher *k* values and more desirable electrical properties.[5, 9] Figure 4.5 shows the dielectric constant measured as a function of frequency up to 1 MHz, with dissipation loss factor D for both cubic and monoclinic films. There is some variation with frequency, as is apparent with the dip in *k* and higher loss D at around 600 kHz due to some parasitic factors. At this point there is a higher loss in the monoclinic thin films, attributed to the polycrystalline nature of the film in which grain boundaries contribute to capacitance leakage. At all frequencies the highly oriented cubic film shows a much greater dielectric constant than the monoclinic films,

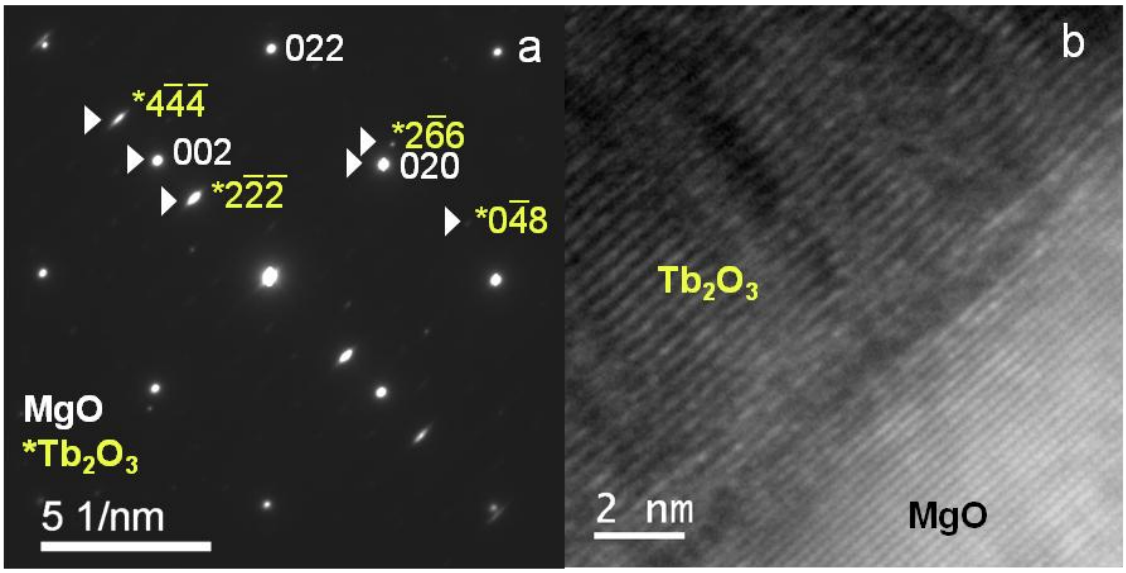

Figure 4.4: Results of TEM characterization. (a) SAD pattern of Tb_2O_3 film on MgO substrate showing film [321] zone axis and substrate [100] zone axis. (b) HRTEM of interface between Tb_2O_3 film on MgO substrate.

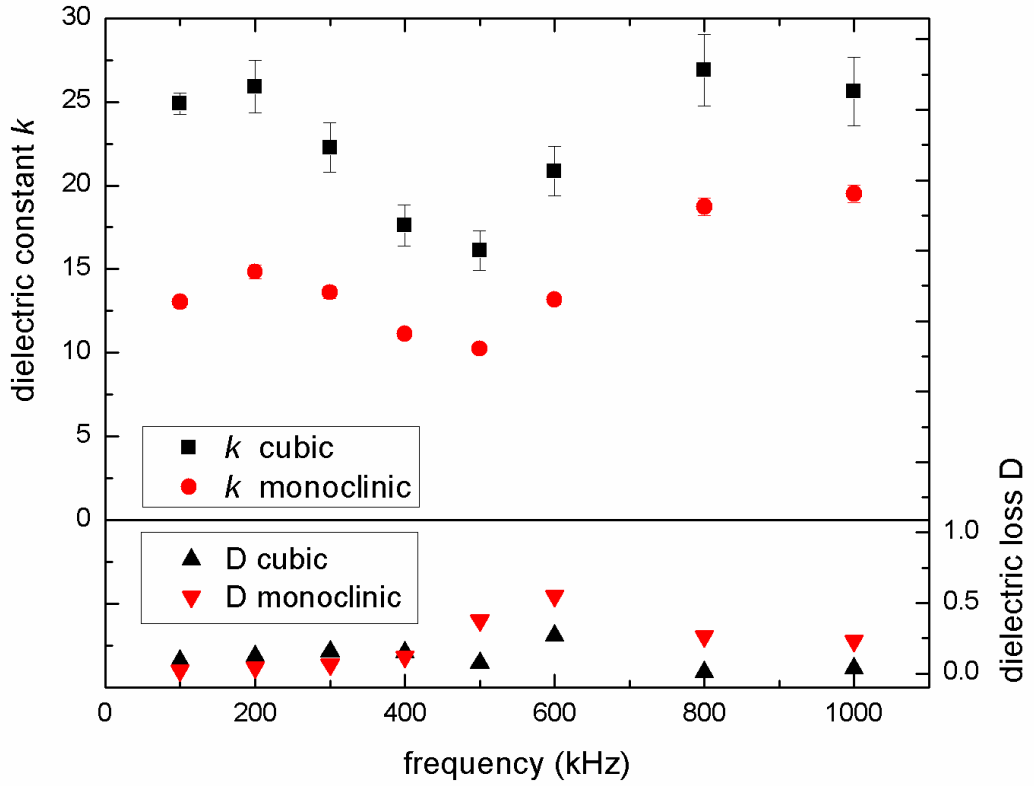

Figure 4.5: Results from dielectric characterization. (top) Dielectric constant measurements of cubic and monoclinic Tb_2O_3 thin films as varied with frequency. Error bars show standard error. (bottom) Dielectric loss D = tan δ for both cubic and monoclinic samples.

and is almost double at low frequencies. The measured dielectric constant of monoclinic Tb_2O_3 is close to the value of bulk Tb_2O_3 previously reported of $k = 13.3$.[11] The highly crystalline cubic thin films show an enhanced $k = 24.9$ at lower frequencies.

4.5 Conclusion

To summarize we have accomplished the PLD growth of high quality Tb_2O_3 thin films with different morphologies and orientations on a variety of substrates including Si. Under high oxygen pressure we have shown the growth of nearly single crystal C-phase thin films, which can be grown either in (001) or (111) orientation depending on the substrate lattice parameter. Using low oxygen pressure a different morphology, B-phase Tb_2O_3 can be achieved. Tb_2O_3 is stable and easy to grow on silicon, and when using PLD at a high relative oxygen pressure the dielectric constant is almost double the reported bulk value and the value of monoclinic phase film of the same composition. This thin film research has not previously been carried out, and will enable further study into direction dependent and strain dependant properties and effects in this material.

4.6 References

1. D. G. Schlom, S. Guha, and S. Datta, MRS Bulletin **33**, 1017 (2008).
2. D. G. Schlom and J. H. Haeni, MRS Bulletin **27**, 198 (2002).
3. K. J. Hubbard and D. G. Schlom, J. Mater. Res. **11**, 2757 (1996).
4. G. Scarel, A. Svane, and M. Fanciulli, Topics in Applied Physics **106**, 1 (2007).
5. Y. Nishikawa, T. Yamaguchi, M. Yoshiki, H. Satake, and N. Fukushima, Appl. Phys. Lett. **81**, 4386 (2002).
6. S. Ohmi, C. Kobayashi, I. Kashiwagi, C. Ohshima, H. Ishiwara, and H. Iwai, J. Electrochem. Soc. **150**, F134 (2003).
7. J. Päiväsaari, M. Putkonen, and L. Niinistö, Thin Solid Films **472**, 275 (2005).
8. A. A. Dakhel, J. Alloys Comp. **365**, 233 (2004).
9. H. Yang, H. Wang, H. M. Luo, D. M. Feldmann, P. C. Dowden, R. F. DePaula, and Q. X. Jia, Appl. Phys. Lett. **92**, 062905 (2008).
10. D. Xue, K. Betzler, and H. Hesse, J. Phys.: Condens. Matter **12**, 3113 (2000).
11. R. D. Shannon, M. A. Subramanian, T. H. Allik, H. Kimura, M. R. Kokta, M. H. Randles, and G. R. Rossman, J. Appl. Phys. **67**, 3798 (1990).
12. H. Ono and T. Katsumata, Appl. Phys. Lett. **78**, 1832 (2001).
13. A. V. Prokofiev, A. I. Shelykh, and B. T. Melekh, J. Alloys Comp. **242**, 41 (1996).
14. L. Petit, A. Svane, Z. Szotek, and W. M. Temmerman, Phys. Rev. B: **72**, 205118 (2005).
15. H. B. Lal and K. Gaur, J. Mater. Sci. **23**, 919 (1988).
16. J. Narayan and B. C. Larson, J. Appl. Phys. **93**, 278 (2003).
17. G. D. Wilk, R. M. Wallace, and J. M. Anthony, J. Appl. Phys. **89**, 5243 (2001).

CHAPTER 5

ROOM TEMPERATURE ELECTRICAL INJECTION AND DETECTION OF SPIN POLARIZED CARRIERS IN SILICON USING MgO TUNNEL BARRIER

5.1 Abstract

We are reporting *room-temperature, all-electrical* injection and detection of spin-polarized carriers in silicon using NiFe/MgO tunnel-barrier-contacts. From the magnetic-field dependence of the spin-accumulation voltage, spin-lifetime and diffusion-length of the carriers were determined to be 276 ps and 328 nm, respectively. For comparison, similar experiments were also performed using NiFe/Al_2O_3 tunnel-barrier-contacts. However, in the latter case spin-lifetime and diffusion-length were found to be lower (~107 ps, 204 nm) demonstrating the superiority of MgO-barrier for spin-injection application. Attaining spin diffusion lengths of >320 nm in Si channels is a ground breaking step and opens tremendous opportunities for integrating spin functionality into post-Moore-era electronic devices.

5.2 Introduction

Spintronics is a fast emerging branch of electronics that utilizes both the charge as well as the spin of electrons. It has the potential to facilitate devices that can store and process information simultaneously, thereby providing superior multifunctional devices with enhanced speed and capacity.[1-4] The most important step in the functioning of a spintronic device is the injection and detection of spin-polarized carriers into the semiconductor channel. Optical techniques were used for the above purposes in most of the work performed till very recently. However, optical methods of injecting spins are not very convenient for fabricating actual devices. Moreover, though optical methods work quite well for direct band-gap semiconductors, the same do not work for the silicon based devices due to the indirect nature of its band-gap. Since silicon is widely regarded as the current workhorse of the electronics industry, researchers are very keen on developing non-optical methods of spin injection and detection for silicon based spintronic devices.

Despite considerable efforts, efficient injection and detection of spins into semiconductors by nonoptical means still continues to be a major hurdle in this field. Ferromagnetic metals such as Fe and Ni were used in earlier studies for injecting spin-polarized carriers into a semiconducting transport medium.[5,6] However, in most of the studies the degree of spin polarization of injected carriers was less than 1%.[7] In order to overcome this, three approaches have been proposed for the efficient injection of spin-polarized carriers into semiconductors: (a) tunneling of spin-polarized carriers from ferromagnetic metals into the semiconductor through an insulator,[8] (b) tunneling of nonpolarized carriers through a ferromagnetic insulator, which acts as a spin filter,[9,10] (c) using dilute magnetic semiconductors (DMS) which are ferromagnetic and whose

conductivity can be tuned to match the nonmagnetic semiconducting transport medium.[11] While the materials needed for testing the feasibility of the last two approaches are still being searched,[12,13] significant progress has been made using the first approach. Hanbicki *et al.*[8] reported 30% spin-polarized injection using the above approach. However, in their work only injection was accomplished using electrical methods, detection of spin polarized carriers was still carried out using optical methods.

Recently in a very interesting report, Dash *et al.*[14] reported the all electrical injection and detection of spin polarized carriers in silicon. This work was performed using Al_2O_3 as the tunneling barrier. However, MgO has been predicted to be a better barrier material compared to Al_2O_3 due to a coherent spin tunneling process.[15,16] For example it has been shown that in Fe/MgO tunneling barriers, Bloch states in the metal couple to evanescent states in the MgO in such a way that the most highly symmetric Bloch states possess the highest tunneling probability.[16] On the other hand, in the case of Al_2O_3 barrier, all Bloch states possess some probability of tunneling, including the ones with greater minority spin populations, so the total tunneling spin polarization is much less compared to the case when MgO barrier is used.[16]

5.3 Experimental Procedure

In this paper, we are reporting the all electrical injection and detection of spin polarized carriers using NiFe/MgO tunnel-barrier-contacts. NiFe/MgO tunnel-barrier-contacts arranged in lateral three-probe-geometry [Fig. 5.1(a)] were fabricated to create and investigate the flow of polarized electrons in silicon. Commercially available p-type silicon-on-insulator wafer with 2 μm thick active silicon layer was used for fabricating the devices. The wafer was oxidized using a wet method to give an 800 nm protective

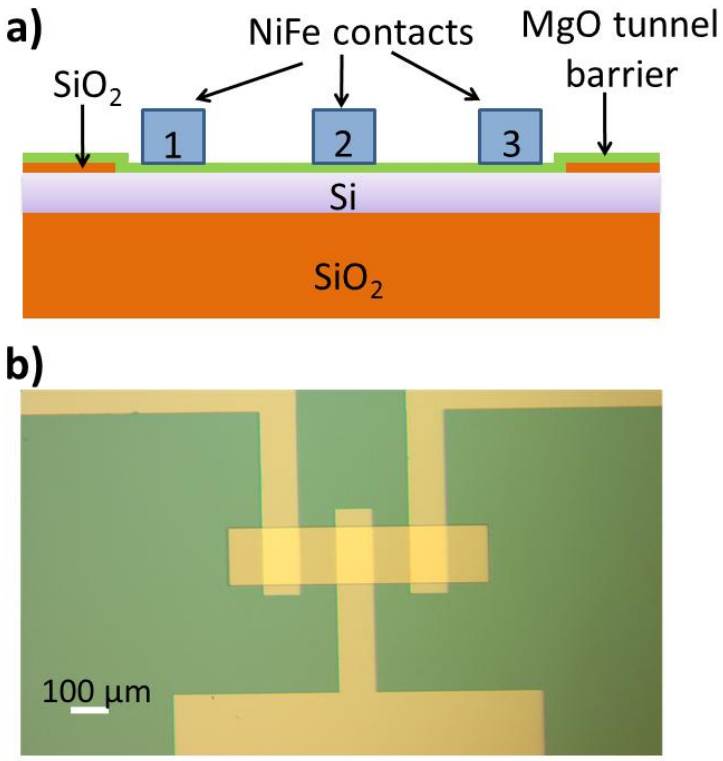

Figure 5.1: Three terminal Hanle device. (a) Schematic diagram illustrating the cross-sectional view of the lateral three-probe test device used in this study, (b) optical micrograph of the test device.

SiO_2 layer. Channels were etched into the SiO_2 layer using HF acid treatment, and the tunnel barrier was deposited. For depositing MgO tunnel barrier layer, MgO ceramic target was placed 4.5 cm from the substrate and ablated using a KrF pulsed excimer laser. Laser energy used for ablation was 150 mJ and laser spot size was 1 mm^2 giving an energy density of 1.5×10^5 J/m^2. With above parameters, 10 pulses of KrF resulted in the deposition of approximately 0.5 nm of MgO onto the Si substrate. For Al_2O_3 tunneling barriers, atomic layer deposition (ALD) was used, and 0.5 nm films were deposited using TMAl and H_2O precursors at 250 °C. After depositing tunnel barrier layers, resulting structures were patterned with photoresist and transferred to an e-beam assisted thermal evaporation chamber, where 20 nm of $Ni_{80}Fe_{20}$ alloy were deposited as ferromagnetic top contact layers. The distance between contacts was kept between 100-200 microns. The optical micrograph of the resulting device is shown in Fig. 5.1(b).

The devices were electrically characterized by passing a constant current of 100 μA across the outer two contacts (terminal 1 and 3), while the voltage drop (V) was measured across one outer and one inner contact (terminal 1 and 2) as illustrated in the insets of Fig. 5.2. Variation of V with the applied transverse magnetic field is shown in Fig. 5.2. Because of the 3-point measurement geometry, the measured voltage (V) is the sum of: (i) the voltage drop across the part of the channel between 1 and 2 (V_C), (ii) voltage drop across the tunnel junction (V_J), (iii) voltage drop due to the spin accumulation beneath the spin injection contact (V_S). Though the contributions coming from the first two terms are straightforward, origin of the third term lies on the spin-dependent tunneling of carriers from the ferromagnetic contact.

The injection of a spin-polarized tunnel current from the ferromagnetic contact

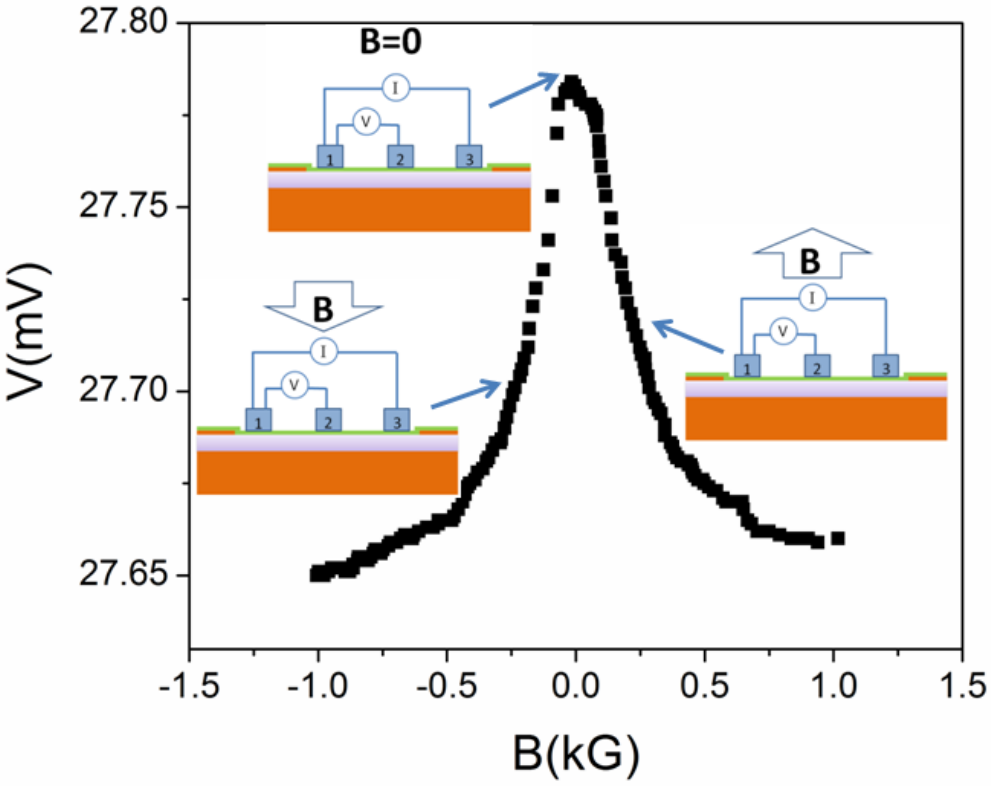

Figure 5.2: Variation of voltage 'V' between the contacts 1 and 2 with magnetic field. A constant current of 100 pA was passed between contacts 1 and 3. Insets show measurement geometry.

into the Si (which is p-type in our case) produces a spin-dependent imbalance in the hole population in the valence band of Si.[17] The above imbalance results in different electrochemical potentials, $\mu\uparrow$ and $\mu\downarrow$, for the up and down spin directions, respectively, and a net spin accumulation, $\Delta\mu = \mu\uparrow - \mu\downarrow$ [see Fig. 5.3(a)]. Spin accumulation is maximum just below the contact and decays as the distance from the interface increases with a spin diffusion length L_{SD}.

The spin accumulation of carriers underneath the contact results in the additional voltage 'V_S' which is related to the spin accumulation, $\Delta\mu$, by the relation[18]:

$$V_S = TSP \times \Delta\mu / 2 \tag{5.1}$$

where TSP is the tunnel spin polarization, a characteristic of the interface. When a magnetic field is applied perpendicular to the carrier spins in the semiconductor channel, spin accumulation and hence the voltage decreases by means of the electrical Hanle effect.[14] Specifically on the application of transverse magnetic field, spins begin precession about this field and the spin accumulation decays [see Fig. 5.3(b)] following the relation:[14]

$$\Delta\mu(B) = \frac{\Delta\mu(0)}{(1+(\omega_L\tau)^2)} \tag{5.2}$$

where τ is the spin lifetime and ω_L is the Larmor frequency given by $\omega_L = 2\pi g\mu_B B/h$, μ_B is the Bohr magneton and g is the Lande´ g-factor, h is planck's constant. The decay in the value of $\Delta\mu$ with transverse magnetic field results in a similar decrease in value of V_S (and hence on the net voltage V):

$$V_S = TSP \times \frac{\Delta\mu(0)}{2(1+(\omega_L\tau)^2)} \tag{5.3}$$

The contributions coming from the V_C and V_J show negligible changes with the

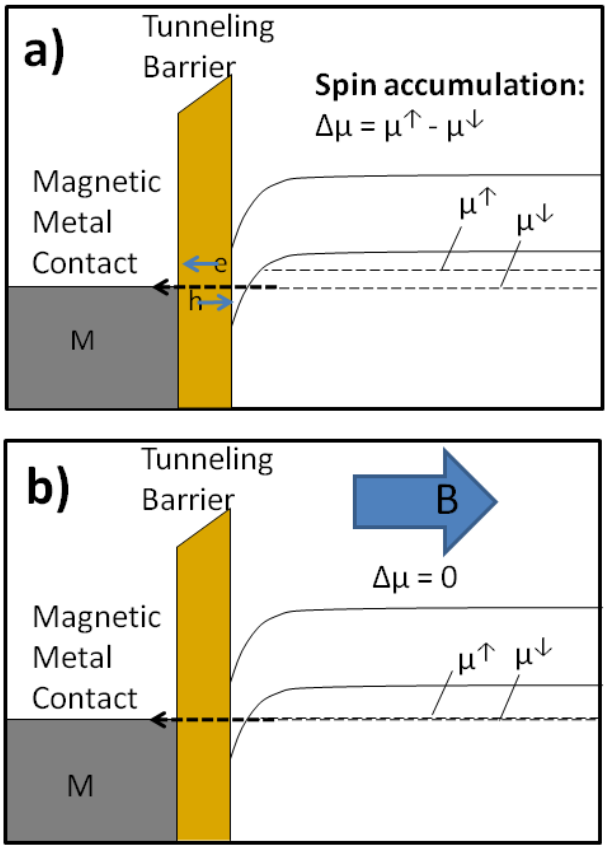

Figure 5.3: Schematic diagram illustrating the injection of charge carriers from ferromagnetic contact to silicon (a) in the absence of any magnetic field, (b) in the presence of a magnetic field perpendicular to the polarization of injected carriers.

applied magnetic field, so the variation in V with B is expected to occur only due to V_S.[14]

5.4 Results and Discussion

Figure 5.4 shows the value of Vs determined from the change in V with B. By fitting V_S to Eq. 5.3, the value of the spin coherence lifetime at room temperature was determined to be 276 picoseconds for NiFe/MgO tunnel contact. Using the experimentally determined electrical resistivity and the Hall effect data, the mobility (μ) of holes was found to be 151 $cm^2V^{-1}s^{-1}$. Using the Einstein relation, $D = \mu k_B T / e$, the diffusion constant (D) was estimated to be 3.9 cm^2s^{-1}. From this the spin diffusion lengths $L_{SD} = \sqrt{D\tau}$ were determined to be 328 nm. These values of diffusion lengths are sufficient to very easily communicate spin information over the typical channel length in the present 32 nm node silicon technology.

For comparison we also fabricated devices with NiFe/Al_2O_3 tunnel-barrier-contacts on the same batch of silicon and performed Hanle effect measurements. Fig. 5.5 shows the variation of spin accumulation voltage with transverse magnetic field. In this case the value of τ was found to be 107 picoseconds. Higher spin lifetime values for MgO/NiFe tunnel contacts compared to that for Al_2O_3/NiFe tunnel contacts, indicate the superiority of MgO barriers for spintronic applications.

5.5 Summary

In summary, we have demonstrated that using MgO barrier in a local three-point device structure, all the three main operations required from a spintronic device i.e. spin injection, detection and manipulation can be accomplished at room temperature in a non-

optical configuration. Diffusion length of carriers injected from NiFe/MgO contact into Si channel was found to be 328 nm, which is good enough to realize room-temperature spintronic devices.

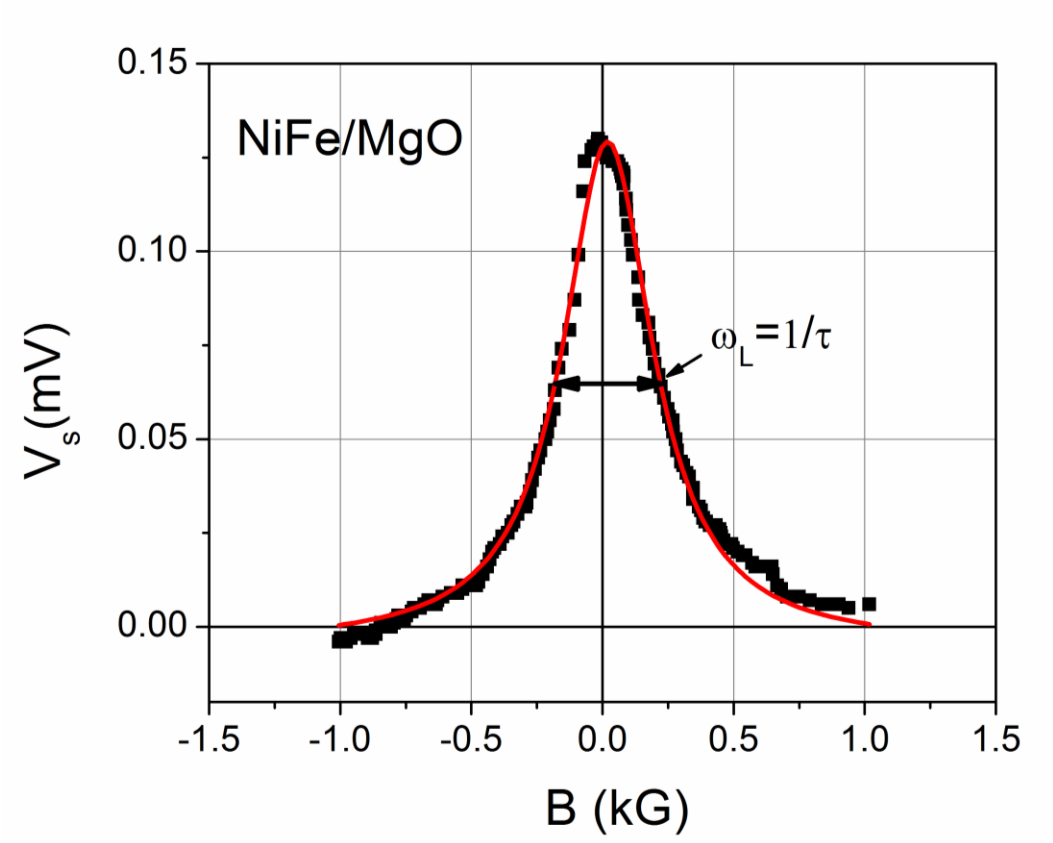

Figure 5.4: Variation of spin accumulation voltage V_S with transverse magnetic field for NiFe/MgO tunnel contacts. Solid line represents fit to eqn. 5.3.

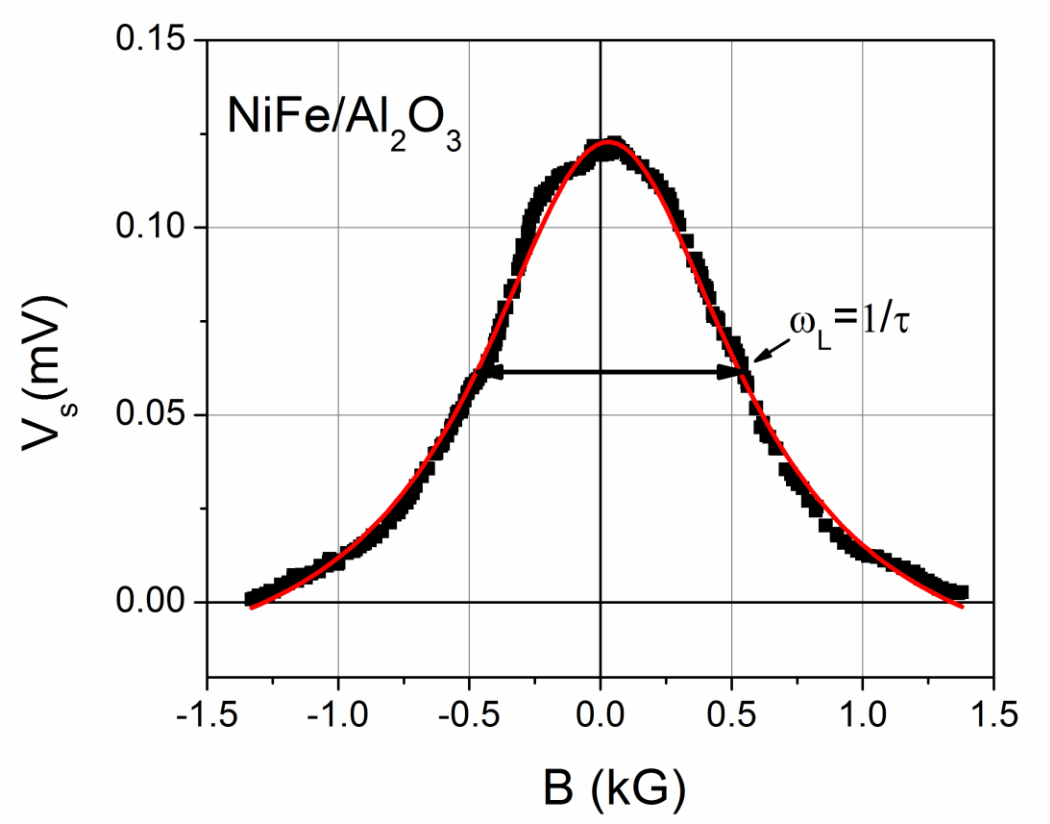

Figure 5.5: Variation of spin accumulation voltage V_S with transverse magnetic field for $NiFe/Al_2O_3$ tunnel contacts. Solid line represents fit to eqn. 5.3.

5.6 References

1. S. A. Wolf, D. D. Awschalom, R. A. Buhrman, J. M. Daughton, S. von Molnar, M. L. Roukes, A. Y. Chtchelkanova and D. M. Treger, Science **294**, 1488 (2001).

2. S. A. Chambers, Materials Today **4,** 34 (2002).

3. S.J. Pearton, D.P. Norton, R. Frazier, S.Y. Han, C.R. Abernathy and J.M. Zavada, IEE Proc-Circuits, Devices and Systems **152**, 312(2005).

4. G. A. Prinz, Science **282**, 1660 (1998).

5. W. Y. Lee, S. Gardelis, B. C. Choi, Y. B. Xu, C. G. Smith, C. H. W. Barnes, D. A. Ritchie, E. H. Linfield and J. A. C. Bland, Journal of Applied Physics **85**, 6682 (1999).

6. P. R. Hammar, B. R. Bennett, M. J. Yang and Mark Johnson, Physical Review Letters **83**, 203 (1999).

7. G. Schmidt, D. Ferrand, L. W. Molenkamp, A. T. Filip and B. J. Van Wees, Phys. Rev. B **62**, R4790 (2000).

8. A. T**.** Hanbicki, B. T. Jonker, G. Itskos, G. Kioseoglou and A. Petrou, Applied Physics Letters **80**, 1240 (2002).

9. X. Hao, J. S. Moodera and R. Meservey, Phys. Rev. B **42**, 8235 (1990).

10. R. Fiederling, M. Keim, G. Reuscher, W. Ossau, G. Schmidt, A. Waag and L. W. Molenkamp, Nature **402**, 787 (1999).

11. G. Schmidt and L. W. Molenkamp, Semiconductor Science and Technology **17**, 310 (2002).

12. M. Snure, D. Kumar and A. Tiwari, Appl. Phys. Lett. **94**, 012510 (2009).

13. C. Liu, F. Yun and H. Morkoc, J. Mater. Sci.: Mater. Electron. **16**, 555 (2005).

14. S. P. Dash, S. Sharma, R. S. Patel, M. P. de Jong and R. Jansen, Nature **462**, 491 (2009).

15. S. S. P. Parkin, C. Kaiser, A. Panchula, P. M. Rice, B. Hughes, M. Samant and S. H. Yang, Nature Mater. **3**, 862 (2004).

16. S. Yuasa, Journal of the Physical Society of Japan, **77**, 031001 (2008).

17. If the Si was n-type, it would produce spin-dependent imbalance in the electron-population.

18. A. Fert and H. Jaffre`s, Phys. Rev. B **64**, 184420 (2001).

CHAPTER 6

ANOMALOUS SPIN TRANSPORT IN ZnO

6.1 Abstract

We report *all-electrical* injection and detection of spin-polarized carriers in ZnO using NiFe/MgO tunnel-barrier-contacts. The three-terminal Hanle effect is used to study spin transport in single crystal thin film ZnO grown on sapphire. The results show that spin injection persists up to and above room temperature, with a measured lifetime τ_s=174 ps at 340K. These results underscore the importance of ZnO as a material for future active spintronics devices.

6.2 Introduction

Zinc oxide (ZnO) has become a highly promising candidate material for applications in the field of spintronics. It is the most widely studied oxide system in the search for dilute magnetic semiconductor (DMS) materials. Since Dietl's 2000 prediction[1] several ZnO based DMS have been reported with extensive magnetic and optical characterization.[2-7] Furthermore, ZnO has a small spin-orbit coupling and relatively few nuclear spins, which is anticipated to contribute to long spin coherence times.[8] Fewer groups have explored the spin transport properties of ZnO, but the results

so far confirm ZnO as a potential spin transport material for proposed spintronics devices. In 2005 it was shown experimentally that ZnO epitaxial films have long coherence times of about 188 ps at about room temperature and 2 ns at 10K.[9] Further research has shown that the spin precession in ZnO can be controlled by a dc "gate" voltage,[10] demonstrating the exciting prospect that the spin-orbit interaction in ZnO can be tuned by an external electronic control. All of these factors make ZnO a very viable material for actual implementation of spin transistors.

Until now the primary research on spin injection and detection in ZnO has been using optical techniques, which are unfavorable for device implementation outside the laboratory. In this paper we report the successful injection and detection of spin current into ZnO using all electrical characterization methods *at and above* room temperature. Spin injection is achieved using ferromagnetic metal/insulating tunnel junction contact.

Significant progress continues to be made by using ferromagnet/tunnel barrier contacts for efficient spin injection into Si and III/V semiconductors. For example Hanbicki *et al.* reported 30% spin-polarized injection into AlGaAs through a tunnel junction.[11] More recently, a number of reports of room temperature spin injection using ferromagnet/tunnel barrier contacts with very long spin diffusion lengths in Si using a three-terminal Hanle measurement.[12-14]

In this work we have made and characterized three-terminal Hanle devices with NiFe/MgO tunnel-barrier contacts to probe the spin transport properties of ZnO. We were able to measure the spin lifetime using all-electrical means at and above room temperature, with the room temperature spin lifetime being τ_s = 79 ps. Remarkably, the measured spin lifetime increases with temperature, reaching τ_s = 174 ps at 340K.

Assuming the room temperature mobility to be $\mu = 4.2$ cm^2/V s the diffusion coefficient $D = \mu kT/q = 0.1086$ cm^2/s and the diffusion length $L = \sqrt{D\tau_s} \approx 43$ nm. The room temperature lifetime measurements corresponds to a diffusion length of charge carriers sufficiently long for modern device dimensions.

6.3 Results and Discussion

We have fabricated NiFe/MgO tunnel-barrier contacts in a three-terminal device geometry [Fig. 6.1] for probing the flow of polarized electrons in ZnO. NiFe magnetic contacts and MgO tunnel barriers were chosen due to the proven success of spin injection with these contacts in similar Si devices,[13] and the coherent tunneling mechanism in MgO enables effective spin transfer.[15] The 300nm ZnO film was deposited by pulsed laser deposition (PLD) onto a single crystal c-plane sapphire (Al_2O_3) substrate held at 600°C in at an oxygen pressure of 10^{-5} bar. The PLD system uses a 248nm KrF pulsed excimer laser, with laser fluence of 15 J/cm^2. ZnO growth was characterized by X-ray diffraction [Fig. 6.2] showing only reflections from the (0002) family of planes from the ZnO film with the (0006) family of planes from the substrate. This indicates that the ZnO crystal is epitaxially oriented with the substrate and of high quality. The optical transmission spectrum of the ZnO thin film on sapphire substrate is shown in Fig. 6.3. The bandgap of the ZnO film was calculated by fitting optical absorbance data to the equation $\alpha = C(h\nu - Eg)^{1/2}$. In this equation C is constant, h is planck's constant, ν is the light frequency, Eg is the bandgap, and the exponent ½ is standard for direct bandgap materials. The bandgap (Eg) was found to be 3.28 eV [see Fig. 6.3 inset].

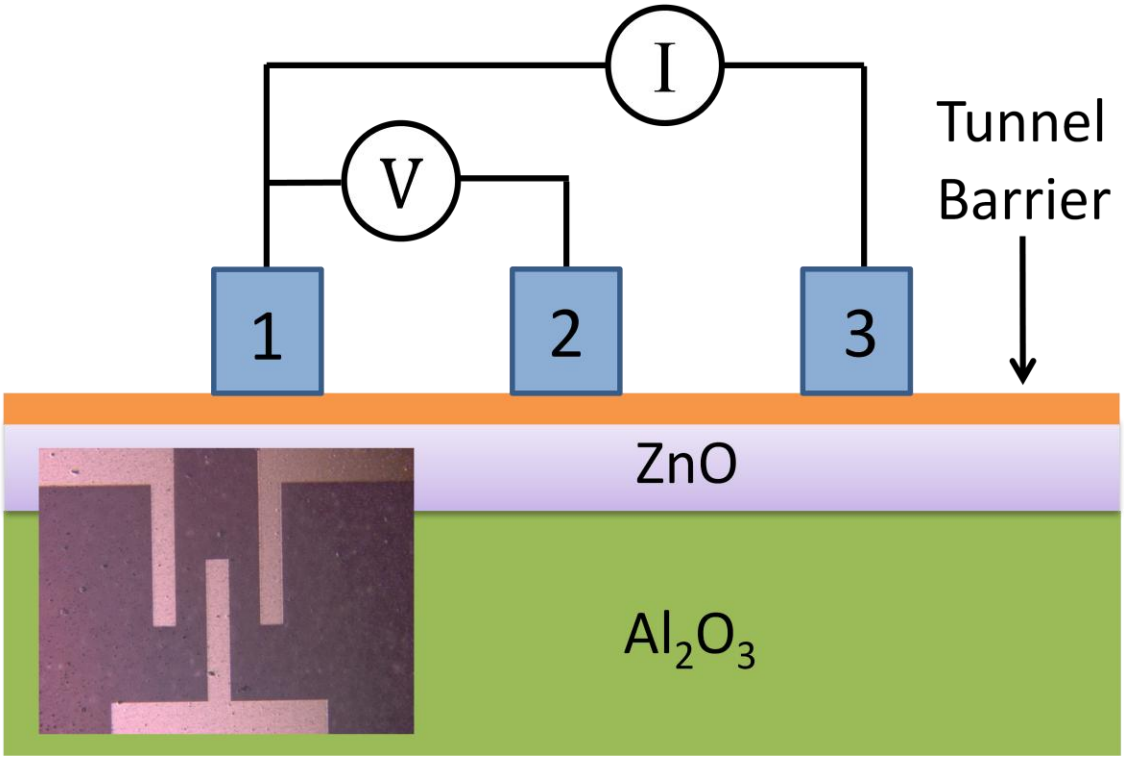

Figure 6.1: Schematic diagram of ZnO channel device with MgO tunnel barrier and three NiFe contact terminals. Inset shows optical micrograph of completed device.

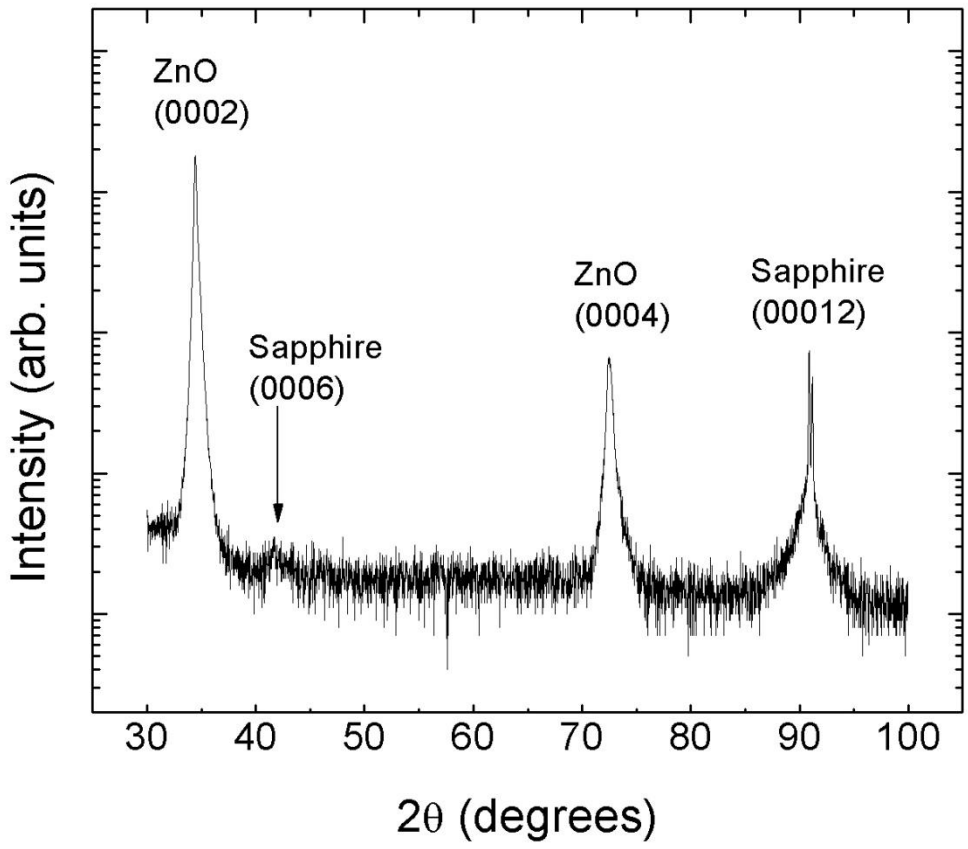

Figure 6.2: θ-2θ x-ray diffraction pattern for ZnO thin film on sapphire substrate, showing single crystalline epitaxial relationship.

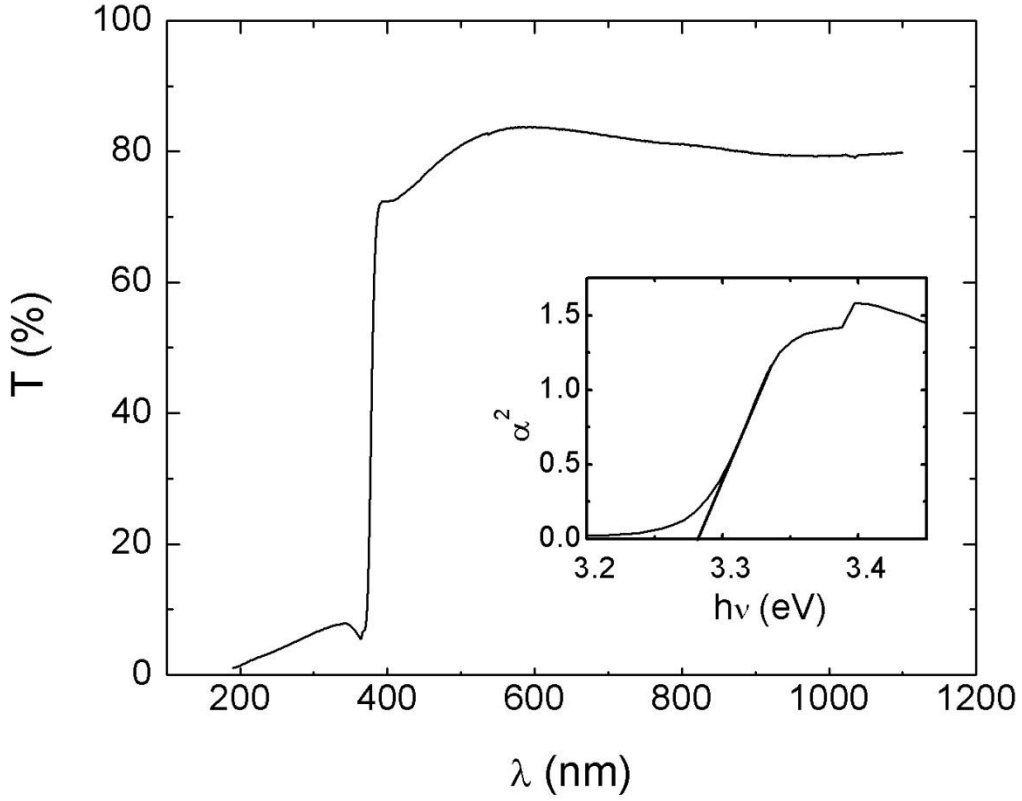

Figure 6.3: UV-Vis spectrum showing the ZnO thin film is transparent to most of the visible spectrum. Inset shows bandgap estimation method: α^2 vs energy is plotted, and the x intercept of the extrapolated linear portion gives the direct bandgap.

Following ZnO layer growth, the ZnO ablation target was exchanged for an MgO target without breaking vacuum, and the oxygen gas was pumped out of the chamber. The substrate was cooled to room temperature, and a thin tunneling barrier layer of MgO was deposited at a vacuum of 10^{-9} bar. The substrate was removed from the vacuum chamber, conventional liftoff photolithography was used to pattern device structure, and samples transferred to an e-beam assisted thermal evaporation chamber. The three ferromagnet top contacts are 20nm thick permalloy ($Ni_{80}Fe_{20}$) 100μm wide. The inset of Fig. 6.1 shows an optical micrograph of the completed device. The contacts are separated by 100 μm spacing, with contact 1 used as spin injector and detector, and contacts 2 and 3 used as references. These contacts were magnetized by elevating the temperature, applying a strong in-plane magnetic field at and cooling the device while maintaining the field.

In the three terminal Hanle measurement the spin-polarized electrons injected into the channel cause an imbalance in the electrochemical potentials of up and down spin electrons.[16,17] The spin accumulation ($\Delta\mu = \mu^{\uparrow}-\mu^{\downarrow}$) is the difference in electrochemical potentials. When a transverse (out-of-plane) magnetic field is applied, spins precess about the field at the Larmor frequency. This precession causes the spins to decohere, reducing the spin accumulation $\Delta\mu$ according to the electrical Hanle effect. The change in voltage signal ΔV is a function of applied field B, and is directly proportional to the spin imbalance $\Delta\mu$ according to the relations:[14,18]

$$V_S = TSP \times \Delta\mu / 2 \tag{6.1}$$

$$V_S(B) = TSP \times \frac{\Delta\mu(0)}{2(1+(\omega_L\tau)^2)} \tag{6.2}$$

where TSP is the tunnel spin polarization, a characteristic of the interface; τ is the spin lifetime, ω_L is the Larmor frequency given by $\omega_L = 2\pi g\mu_B B/h$; μ_B is the Bohr magneton, g is the Lande´ g-factor, and *h* is Planck's constant.

Three terminal Hanle measurements were used to determine the spin lifetime τ_s. A constant current of 100 μA was passed across terminals 1 and 3 and the voltage was measured across terminals 1 and 2 as a transverse magnetic field was swept in both directions. The room temperature (T=300K) Hanle data are shown in Fig. 6.4. Spin coherence lifetime was calculated by setting τ as a free parameter and fitting the voltage vs. field data to Eq. 6.2. Using this method the room temperature spin lifetime was calculated to be τ_s = 79 ps.

Before fitting, the raw data (shown in the inset of Fig. 6.4) was translated slightly along the x-axis to compensate for a hysteretic response that split the peak maxima. The origin of this shift likely arises due to a small out-of-plane component of the magnetic moment of the top contacts. The moment opposes the applied field at low levels and aligns with it at high levels. If these contacts were infinitesimally thin we should not see any splitting, and after translating the data and averaging both sides the curve agrees very well with Eq. 6.2, especially at lower fields.

Using the same method, measurements were made at increased temperatures, with a Hanle response up to 340K. Surprisingly, the measured spin lifetime at T=340K is τ_s=174 ps, which is higher than the room temperature value (see Fig. 6.5). This trend confirms research reported by Ghosh *et al*. showing an increasing trend in temperature dependence of τ_s in the high temperature regime using optical methods for measurement.[9]

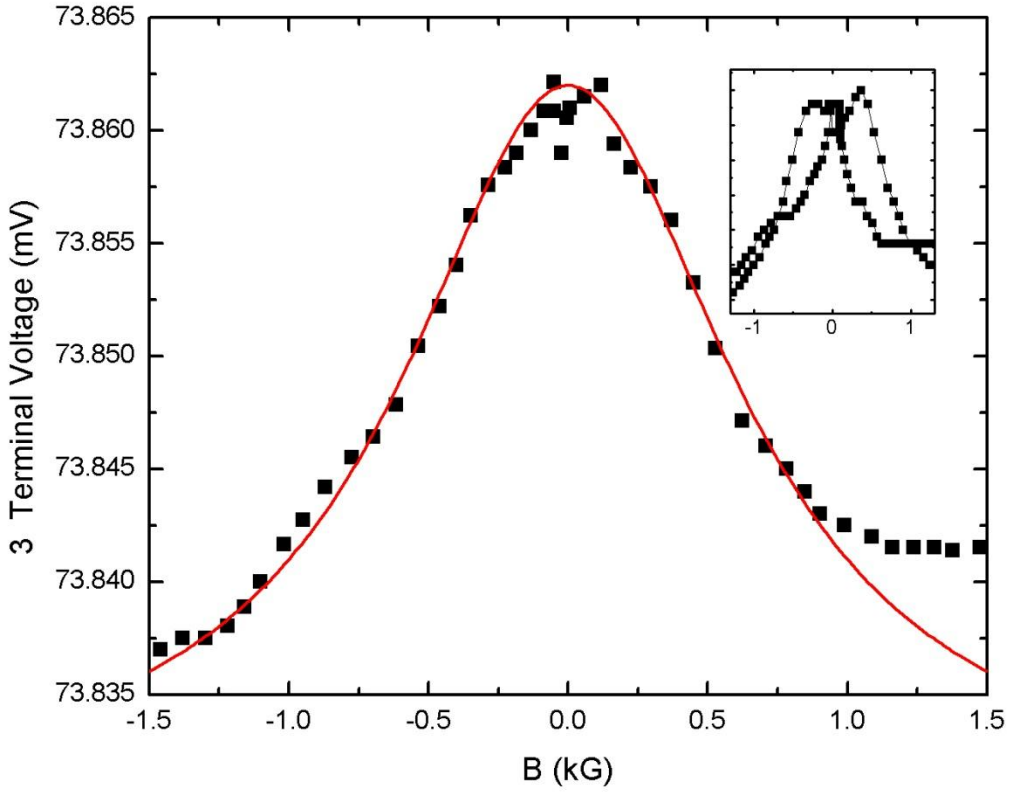

Figure 6.4: Variation in spin accumulation voltage V_S with transverse magnetic field at temperature T = 300K, with spin life τ_s = 79ps. Solid line represents fit to Eq. 6.3. Inset shows original data before remanent field correction.

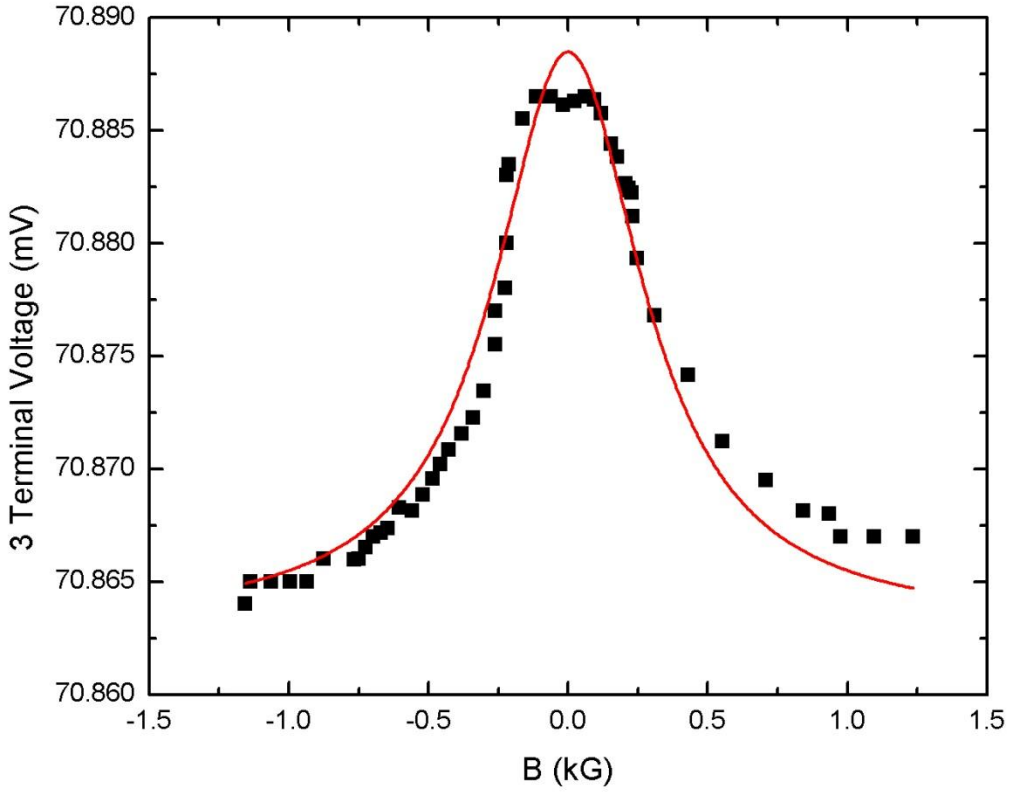

Figure 6.5: Variation in spin accumulation voltage V_S with transverse magnetic field at temperature T = 340K, with spin life τ_s = 174ps. Solid line represents fit to Eq. 6.3.

Our observed lifetime is reduced compared with the Ghosh report of τ_s = 188 ps at 280K, so some loss of accuracy and the differing injection conditions contribute to reduce the measured value, although not significantly. Further, the values reported using the Hanle method are typically considered a lower boundary to the actual lifetime, so these reported values should be considered as minimum limits.[14]

In addition to the Elliot-Yafet and D'yakonov- Perel scattering theories some other mechanism is dominating the high temperature behavior of the ZnO system. We have shown that this unexplained phenomenon persists even above room temperature.

6.4 Summary

In summary, we have demonstrated high spin coherence values up to 340K using all-electrical injection and detection of spin polarized current in ZnO thin films. This further sets ZnO apart as a viable and promising material in which future spin devices can become a reality.

6.5 References

1. T. Dietl, H. Ohno, F. Matsukura, J. Cibert, and D. Ferrand, Science **287**, 1019 (2000).

2. K. Ueda, H. Tabata, and T. Kawai, Appl. Phys. Lett. **79**, 988 (2001).

3. M. Snure and A. Tiwari, J. Appl. Phys. **106**, 043904 (2009).

4. N. H. Hong, V. Brize, and J. Sakai, Appl. Phys. Lett. **86**, 082505 (2005).

5. M. Venkatesan, C. B Fitzgerald, J. G. Lunney, and J. M. D. Coey, Phys. Rev. Lett. **93**, 177206 (2004).

6. S. Singh, N. Rama, K. Sethupathi, and M. S. Ramachandra Rao, J. Appl. Phys. **103**, 07D108 (2008).

7. D. L. Hou, X. J. Ye, X. Y. Zhao, H. J. Meng, H. J. Zhou, X. L. Li, and C. M. Zhen J. Appl. Phys. **102**, 033905 (2007).

8. V. Sih, S. Ghosh, D. Awschalom, S. Bae, S. Wang, G. Chapline, S. Vaidya, http://meetings.aps.org/link/BAPS.2005.MAR.J10.5

9. S. Ghosh, V. Sih, W. H. Lau, D. D. Awschalom, S. Y. Bae, S. Wang, S. Vaidya, and G. Chapline, Appl. Phys. Lett. **86**, 232507 (2005).

10. S. Ghosh, D. W. Steuerman, B. Maertz, K. Ohtani, H. Xu, H. Ohno, and D. D. Awschalom, J. Appl. Phys. **92**, 162109 (2008).

11. A. T**.** Hanbicki, B. T. Jonker, G. Itskos, G. Kioseoglou and A. Petrou, Appl. Phys. Lett. **80**, 1240 (2002).

12. K. Jeon, B. Min, I. Shin, C. Park, H. Lee, Y. Jo, and S. Shin, Appl. Phys. Lett. **98** 262102 (2011).

13. N. W. Gray and A. Tiwari, Appl. Phys. Lett. **98**, 102112 (2011).

14. S. P. Dash, S. Sharma, R. S. Patel, M. P. de Jong, and R. Jansen, Nature London **462**, 491 (2009).

15. S. Yuasa, J. Phys. Soc. Jpn. **77**, 031001 (2008).

16. Lou, X. C. Adelmann, M. Furis, S. A. Crooker, C. J. Palmstrøm, and P. A. Crowell, Phys. Rev. Lett. 96, 176603 (2006).

17. Tran, M. H. Jaffrès, C. Deranlot, J.-M. George, A. Fert, A. Miard, and A. Lemaître, Phys. Rev. Lett. 102, 036601 (2009).

18. A. Fert and H. Jaffrès, Phys. Rev. B **64**, 184420 (2001)

CHAPTER 7

CONCLUDING REMARKS

This work outlines research into two major topics to further the field of spintronics. Rare earth oxides were explored to determine their viability as dilute magnetic dielectrics for tunnel barrier injection. In addition, Si and ZnO channel materials were both investigated to determine the spin coherence length using traditional (nonmagnetic) tunnel barrier contacts. Based on the results and observations in these studies, the following conclusions were drawn:

7.1 Effects of Cobalt Doping in Sm_2O_3

$Sm_{1.9}Co_{0.1}O_3$ was studied to determine the magnetic response, and then explain the origin of the observed response. Since only intrinsically magnetic materials are useful in tunneling applications, the primary task was to study the incorporation of cobalt into the Sm_2O_3 matrix so as to learn whether the magnetic response was an intrinsic property of the new solid solution, or whether cobalt precipitates had formed and were responsible for the induced magnetic response. After thorough XRD and TEM analysis of the films it was determined that the magnetic response was indeed intrinsic to the material, but the origin of the response was found to be unique to this materials system.

The magnetic response was specifically due to clusters of defects mediating magnetic exchange between uniformly dispersed cobalt dopant ions via polarons. Because the polaron radius is temperature dependant, the cluster size and number was also found to vary with temperature. This magnetic phase was termed "dynamic super-paramagnetism" due to the temperature dependent nature of the clusters. The response was enhanced in monoclinic phase $Sm_{1.9}Co_{0.1}O_3$ as compared with cubic phase $Sm_{1.9}Co_{0.1}O_3$, due to a lower degree of crystallinity resulting in more exchange mediating polarons.

Future work regarding this material could benefit greatly from analysis with additional characterization techniques including magnetic force microscopy (MFM) to ensure uniform magnetic response throughout the sample on the microscale. Electron energy loss spectroscopy can provide chemical composition maps on the nanoscale to ensure homogeneous distribution of the dopant. These would dispel doubts and provide additional insight regarding our interpretation of the dynamic superparamagnetic response. With this knowledge it might be possible to engineer the material such that the the magnetic response is enhanced at room temperature.

7.2 Growth and Characterization of Tb_2O_3 Thin Films

Tb_2O_3 is another good rare earth candidate for magnetic doping to engineer new dilute magnetic dielectrics. However, before doping in magnetic impurities an initial study about the growth, morphology, and properties of thin films for this material needed to be carried out, since very little of this research had been performed before. Therefore, the work reported in this paper gives the results of how growth conditions and substrates

affect the optical, structural, and dielectric properties of thin films of Tb_2O_3. As an added bonus, it was confirmed that high quality cubic crystal Tb_2O_3 exhibits a much higher dielectric constant than previous polycrystalline and bulk values have been reported, which may make Tb_2O_3 a candidate as high-k dielectric replacement for SiO_2 in CMOS applications.

The next step of this research is to explore doping magnetic elements into the Tb_2O_3 thin film in the hopes of developing another new DMD.

7.3 Spin Injection into Silicon with Tunnel Barrier Contacts

Our research also explored spin injection into silicon to determine the spin coherence length of charge carriers when using two types of tunneling barriers. We found that when using MgO tunnel barriers, which is predicted to have better injection efficiency, the coherence length was also improved when compared with Al_2O_3 tunneling barriers. This surprising result may be explained by effects of the quality and type of tunnel barrier material on interfacial/surface states affecting the conduction channel. The most important conclusion was that the coherence length observed at room temperature were 328 nm, much greater than the length of current state-of-the-art transistor devices.

Future research here should involve 4-probe measurements, which will confirm the coherence lengths and prove that localized interface states are not contributing to an artificially high lifetime measurement.

7.4 Spin Injection into ZnO with Tunnel Barrier Contacts

ZnO is a very versatile material and has been predicted to have high spin coherence times for spintronics applications. Taking what we learned from spin injection into silicon we have applied MgO tunnel barrier contacts to ZnO thin films in order to measure the spin coherence time. The coherence time was found to be 79 ps at room temperature, and actually increase to 174 ps at slightly elevated temperatures. This confirms results obtained in other optical injection studies, but as yet is not fully explained.

The next requirement for further development of this material should involve a computational treatment of the spin coherence times in order to gain a working understanding of the dominant scattering mechanism responsible for the unexpected temperature dependence of spin coherence time.